Cell Reports

Article

Mechanosensitive ACKR4 scavenges CCR7 chemokines to facilitate T cell de-adhesion and passive transport by flow in inflamed afferent lymphatics

Graphical abstract

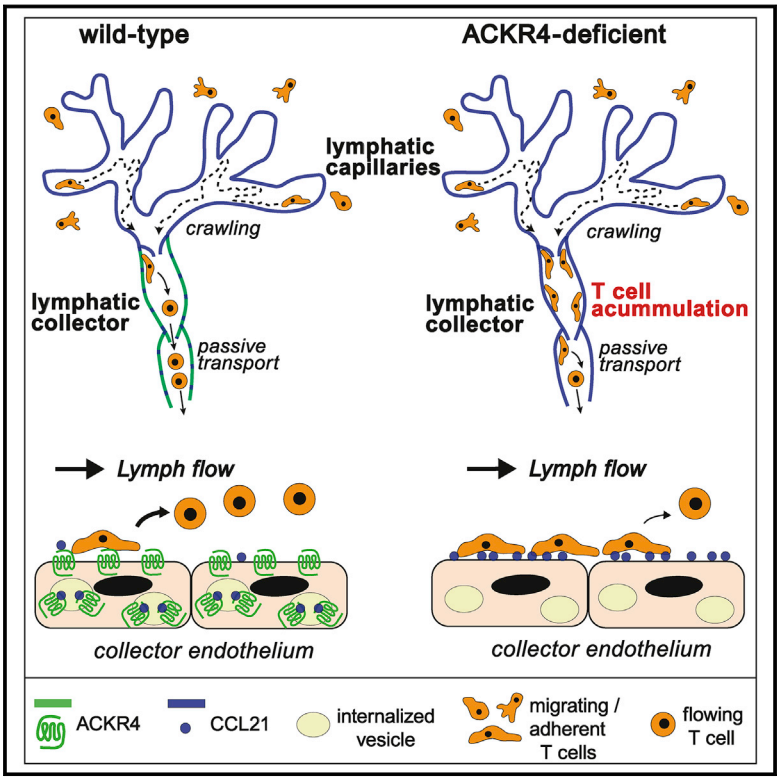

Highlights

- ACKR4 is expressed in a flow-dependent manner in afferent lymphatic collectors
- ACKR4 scavenges CCR7 ligands like CCL21 and removes them from the collector surface
- Chemokine scavenging prevents T cell accumulation in inflamed dermal collectors
- In the absence of ACKR4, T cell migration to draining lymph nodes is reduced

Authors

Mona C. Friess, Ioannis Kritikos, Philipp Schineis, ..., Daniel F. Legler, Tatiana V. Petrova, Cornelia Halin

Correspondence

cornelia.halin@pharma.ethz.ch

In brief

Friess et al. report that ACKR4 is expressed in a flow-dependent manner in afferent lymphatic collectors, where it removes CCR7 ligands from the collector surface. In inflammation, migrating T cells accumulate in dermal ACKR4-deficient collectors and fail to efficiently de-adhere for flow-mediated, passive transport to draining lymph nodes.

Friess et al., 2022, Cell Reports *38*, 110334
February 1, 2022
https://doi.org/10.1016/j.celrep.2022.110334

CellPress

Cell Reports

CellPress
OPEN ACCESS

Article

Mechanosensitive ACKR4 scavenges CCR7 chemokines to facilitate T cell de-adhesion and passive transport by flow in inflamed afferent lymphatics

Mona C. Friess,[1,10] Ioannis Kritikos,[1,10] Philipp Schineis,[1] Jessica Danielly Medina-Sanchez,[1] Anastasia-Olga Gkountidi,[1] Angela Vallone,[1] Elena C. Sigmund,[1] Corina Schwitter,[1] Martina Vranova,[1] Christoph Matti,[2] Jorge Arasa,[1] Cansaran Saygili Demir,[3] Esther Bovay,[3] Steven T. Proulx,[1,4] Michio Tomura,[5] Antal Rot,[6,7,8] Daniel F. Legler,[2,4,9] Tatiana V. Petrova,[3] and Cornelia Halin[1,11,*]

[1]Institute of Pharmaceutical Sciences, ETH Zurich, Zurich, Switzerland
[2]Biotechnology Institute Thurgau (BITg) at the University of Konstanz, Kreuzlingen, Switzerland
[3]Department of Oncology, University of Lausanne and Ludwig Institute for Cancer Research, Lausanne, Epalinges, Switzerland
[4]Theodor Kocher Institute, University of Bern, Bern, Switzerland
[5]Osaka Ohtani University, Osaka, Japan
[6]Centre for Microvascular Research, William Harvey Research Institute, Barts and The London School of Medicine and Dentistry, Queen Mary University of London, London, UK
[7]Centre for Inflammation and Therapeutic Innovation, Queen Mary University London, London, UK
[8]Institute for Cardiovascular Prevention, Ludwig-Maximilians University, Munich, Germany
[9]Faculty of Biology, University of Konstanz, Konstanz, Germany
[10]These authors contributed equally
[11]Lead contact
*Correspondence: cornelia.halin@pharma.ethz.ch
https://doi.org/10.1016/j.celrep.2022.110334

SUMMARY

T cell migration via afferent lymphatics to draining lymph nodes (dLNs) depends on expression of CCR7 in T cells and CCL21 in the lymphatic vasculature. Once T cells have entered lymphatic capillaries, they slowly migrate into contracting collecting vessels. Here, lymph flow picks up, inducing T cell detachment and rapid transport to the dLNs. We find that the atypical chemokine receptor 4 (ACKR4), which binds and internalizes CCL19 and CCL21, is induced by lymph flow in endothelial cells lining lymphatic collectors, enabling them to scavenge these chemokines. In the absence of ACKR4, migration of T cells to dLNs in TPA-induced inflammation is significantly reduced. While entry into capillaries is not impaired, T cells accumulate in the ACKR4-deficient dermal collecting vessel segments. Overall, our findings identify an ACKR4-mediated mechanism by which lymphatic collectors facilitate the detachment of lymph-borne T cells in inflammation and their transition from crawling to free-flow toward the dLNs.

INTRODUCTION

Afferent lymphatic vessels transport soluble antigens and leukocytes, thereby functioning as crucial immunologic connections between peripheral tissues and draining lymph nodes (dLNs). In the skin, they start as blind-ended capillaries, which merge into lymphatic tissue collectors and subsequently into larger collectors that connect to dLNs (Collado-Diaz et al., 2021; Gonzalez-Loyola and Petrova, 2021; Permanyer et al., 2018). Dendritic cells (DCs) and antigen-experienced T cells are the main cell types migrating through afferent lymphatics in steady state and, at an enhanced rate, in inflammation (Collado-Diaz et al., 2021; Permanyer et al., 2018). Under inflammatory conditions, this migration relies on integrins and the integrin ligands ICAM-1 and VCAM-1, which are upregulated in inflamed lymphatics (Arasa et al., 2021; Johnson et al., 2006; Teijeira et al., 2017; Vigl et al., 2011). Conversely, in steady state, when afferent lymphatics express virtually no ICAM-1 and VCAM-1, DC migration occurs independently of integrins (Lämmermann et al., 2008). DC and T cell migration to dLNs also highly depends on the chemokine receptor CCR7 (Bromley et al., 2005, 2013; Debes et al., 2005; Förster et al., 1999). The two known CCR7 ligands are CCL21 and CCL19. CCL21 is constitutively expressed by lymphatic endothelial cells (LECs) in capillaries and less in collectors (Arasa et al., 2021; Russo et al., 2016; Weber and Sixt, 2013), whereas CCL19 is upregulated in activated DCs (Bruckner et al., 2012; Luther et al., 2000; Ngo et al., 1998b; Sallusto et al., 1999b).

CCL21 guides DCs and T cells during several steps of their migration to dLNs. The chemokine's positively charged C terminus confers binding to extracellular proteoglycans such as endothelial cell-expressed heparan sulfates (de Paz et al., 2007; Hirose et al., 2002; Patel et al., 2001). This creates an immobilized peri-lymphatic CCL21 gradient that directs DC migration toward and into lymphatic capillaries (Tal et al., 2011; Weber

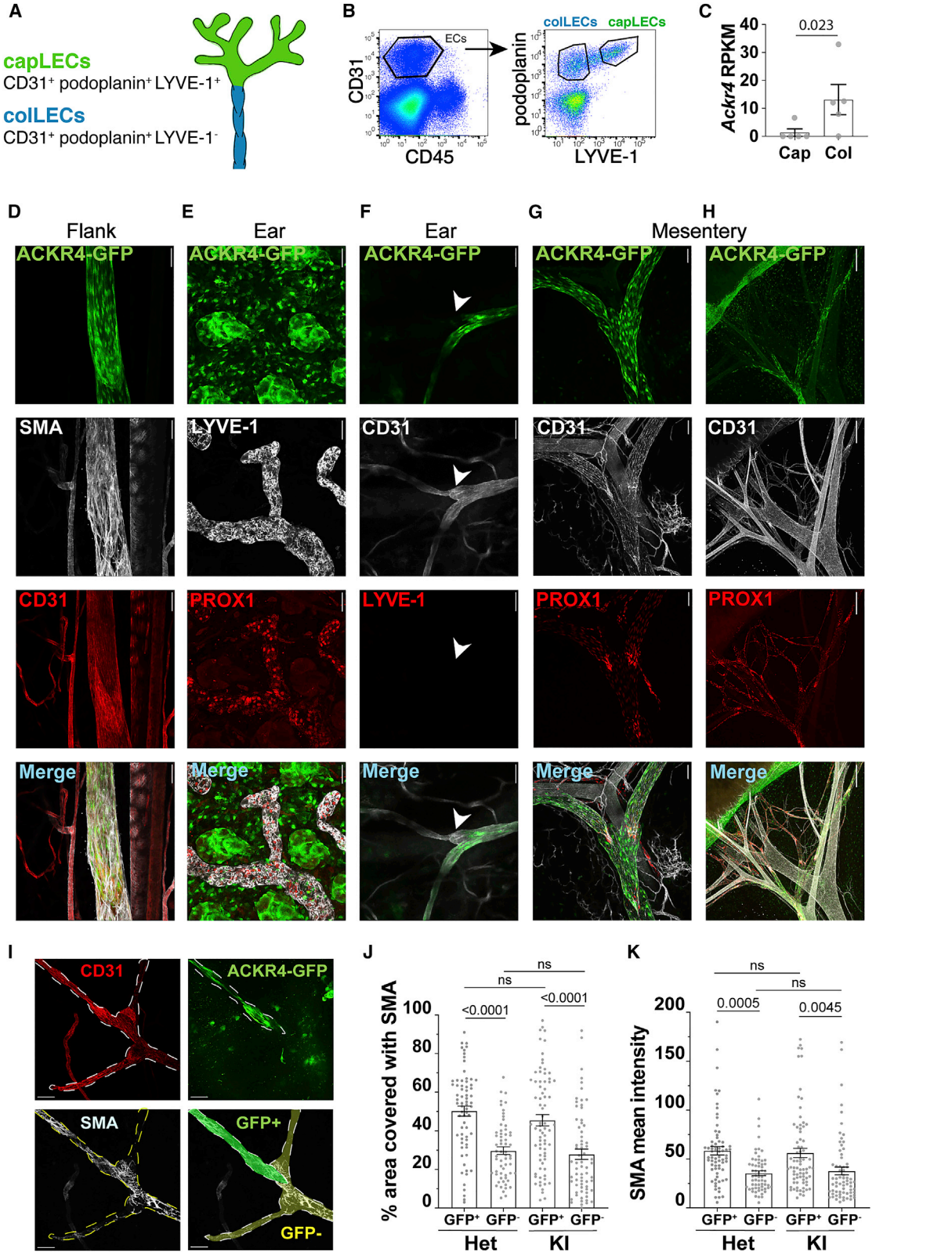

(legend on next page)

et al., 2013). Within lymphatic capillaries, both DCs and T cells actively crawl and patrol, since lymph flow is too low to sustain their passive transport (Russo et al., 2016; Teijeira et al., 2017). Our laboratory has shown that lymph flow establishes a CCL21 gradient within lymphatic capillaries, which supports semi-directed crawling of DCs from capillaries toward lymphatic collectors (Russo et al., 2016). In collectors, where flow picks up due to contractions of the vessel-surrounding lymphatic muscle cells (LMCs), DCs and T cells detach and are rapidly and passively transported with the lymph flow to the dLN (Russo et al., 2016; Tal et al., 2011; Teijeira et al., 2017). Since leukocytes greatly accelerate once they transition from active migration to passive flow (50- to 10,000-fold; Collado-Diaz et al., 2021), de-adhesion in collectors is crucial for efficient propagation of leukocytes to dLNs. Upon arrival in the LN subcapsular sinus (SCS), DCs migrate along yet another CCL21 gradient across the SCS floor into the CCL19-/CCL21-rich LN parenchyma (Ulvmar et al., 2014). By contrast, CCR7 is dispensable for T cell exit from the SCS but required for directional migration within the parenchyma toward the T cell zone (Braun et al., 2011; Martens et al., 2020).

In addition to conventional chemokine receptors, atypical chemokine receptors (ACKRs) regulate the migration of leukocytes in tissues and in the vasculature. ACKRs structurally resemble classical G protein-coupled receptors but, unlike conventional chemokine receptors, do not directly induce migration. Rather, ACKRs are typically expressed by stromal cells and impact leukocyte migration by transporting, presenting, or scavenging chemokines (Nibbs and Graham, 2013; Ulvmar et al., 2011). ACKR4 is one out of four so far described ACKRs and binds the CCR7 ligands, CCL19 and CCL21, as well as some further chemokines (i.e., CCL25 [Gosling et al., 2000], CCL20 [Matti et al., 2020a], and CCL22 [Meyrath et al., 2021]). Its function consists in binding and scavenging its ligands and submitting them to intracellular degradation (Nibbs and Graham, 2013). ACKR4 was shown to promote T cell homing to the spleen (Werth et al., 2021) and to regulate distinct steps in DC migration. In the skin it is expressed by keratinocytes and subsets of fibroblasts and LECs (Bastow et al., 2021; Bryce et al., 2016). In the absence of ACKR4, migration of dermal DCs and Langerhans cells to dLNs was reduced (Bastow et al., 2021; Bryce et al., 2016). Loss of ACKR4 was shown to modulate the peri-lymphatic CCL21 gradient, resulting in less DCs entering into afferent lymphatics (Bastow et al., 2021). On the other hand, the skin egress phenotype observed in ACKR4-deficient mice was completely rescued in CCL19/ACKR4 double-deficient mice (Bryce et al., 2016), suggesting that ACKR4-mediated scavenging of CCL19, which is produced by maturing DCs (Luther et al., 2000; Ngo et al., 1998a; Sallusto et al., 1999a; Vissers et al., 2001), allows DCs to better sense the remaining peri-lymphatic CCL21 gradient during their migration into dermal lymphatics (Bryce et al., 2016). Besides affecting DC migration in the skin, ACKR4 is important for DC exit from the SCS. Specifically, ACKR4 expression in LECs lining the LN SCS was shown to establish a CCL21 gradient, which DCs require for entering the CCL21-producing LN parenchyma (Ulvmar et al., 2014). In contrast to DCs, the involvement of ACKR4 in T cell trafficking to dLNs has not been investigated to date.

This study was sparked by a transcriptomics analysis from our lab (Arasa et al., 2021) suggesting ACKR4 expression in LECs isolated from murine dermal lymphatic collectors, i.e., the vessel segments in which leukocytes transition from active migration to passive transport by flow. Considering that this process so far is completely unexplored, we here set out to investigate the functional significance of ACKR4 expression in lymphatic collectors. Our findings identify ACKR4 as a flow-induced scavenger of CCR7 ligands, which under inflammatory conditions supports T cell migration to dLNs, by facilitating T cell de-adhesion in dermal collectors.

RESULTS

ACKR4 is expressed in afferent and efferent lymphatic collectors

A recent RNA sequencing study from our lab (Arasa et al., 2021) performed on FACS-sorted dermal LECs had indicated higher *Ackr4* expression in CD31$^+$podoplanin$^+$LYVE-1$^-$ collector-derived LECs (colLECs) compared with CD31$^+$podoplanin$^+$ LYVE-1$^+$ capillary-derived LECs (capLECs) (Figures 1A–1C). To further explore ACKR4 expression in afferent lymphatics, we made use of ACKR4 knockin mice, in which the gene encoding ACKR4 is replaced by green fluorescent protein (GFP) (Heinzel et al., 2007). While heterozygous mice (ACKR4$^{GFP/+}$ Het mice) reliably report ACKR4 expression (Bryce et al., 2016; Heinzel

Figure 1. ACKR4 is expressed in a subset of dermal and mesenteric afferent lymphatic collectors

(A) Schematic depiction of the dermal lymphatic vasculature, comprising LECs in lymphatic capillaries (capLECs: CD31$^+$podoplanin$^+$LYVE-1$^+$) and collectors (colLECs: CD31$^+$podoplanin$^+$LYVE-1$^-$).

(B) FACS sorting strategy.

(C) Analysis of *Ackr4* expression (RPKM values) in RNA sequencing performed on capLECs and colLECs (Arasa et al., 2021) (n = 5 mice). p values generated by the DESeq2 package.

(D–H) Tissues from ACKR4$^{GFP/GFP}$ KI mice were prepared as whole mounts, stained for CD31 (pan-endothelial), PROX1 (pan-lymphatic), LYVE-1 (lymphatic capillaries), or SMA (lymphatic collectors), and analyzed by confocal microscopy. Analysis of AKCR4 expression in (D) large efferent collector in the flank, (E) capillaries of the upper ear skin, (F) collectors in the lower ear skin, and (G) in the mesentery. Scale bars, 50 μm in (D–G). White arrow in (F) indicates a valve. (H) Lower magnification confocal image of a mesentery whole mount of ACKR4$^{GFP/+}$ Het mouse stained for PROX1. Scale bars, 200 μm. Representative images from at least two experiments per condition are shown.

(I–K) ACKR4^{GFP} collectors display a denser SMA coverage. Ear skin whole mounts from ACKR4$^{GFP/GFP}$ KI and ACKR4$^{GFP/+}$ Het mice were stained for the endothelial marker CD31 and SMA. (I) The collector region of interest (ROI) was identified by CD31 staining and vessel morphology and subsequently subdivided into ACKR4^{GFP}-positive and ACKR4^{GFP}-negative sub-ROIs, in which (J) the percentage SMA coverage and (K) the mean intensity of the SMA staining were analyzed. Shown are mean ± SEM of pooled data from 3 independent experiments with a total of 5–6 ears per group (with 6–25 images per ear). Each dot corresponds to 1 image analyzed. Statistics: one-way ANOVA with Bonferroni corrections. Scale bars, 50 μm in (I).

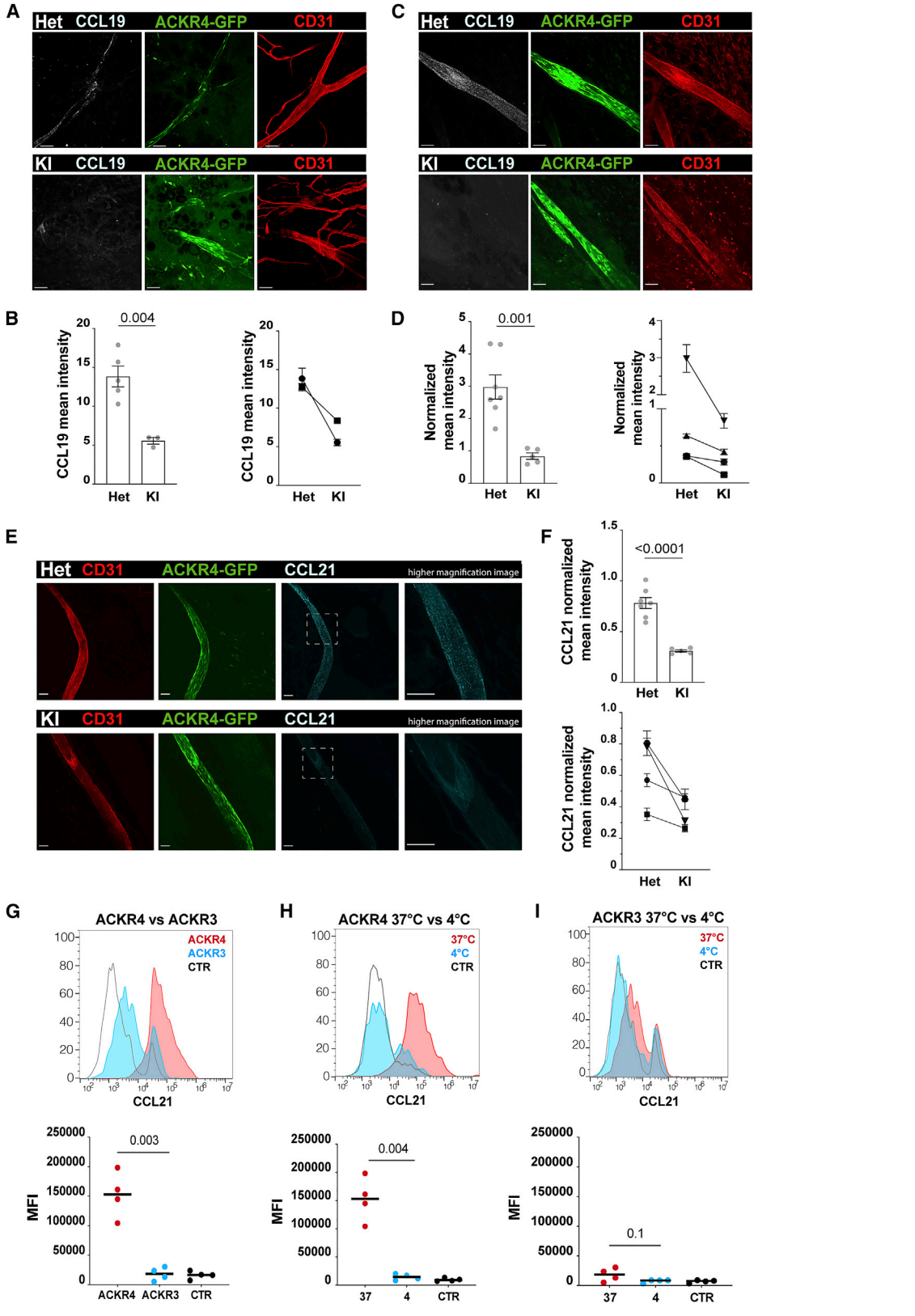

(legend on next page)

et al., 2007; Ulvmar et al., 2014), homozygous mice with GFP knockin into both alleles (ACKR4$^{GFP/GFP}$ KI mice) represent functional knockouts. ACKR4$^{GFP/GFP}$ KI mice displayed a normal body weight, spleen, and LN cellularity (Figures S1A–S1E). However, in agreement with a previous report (Comerford et al., 2010), we detected higher CCL21 levels in serum of ACKR4$^{GFP/GFP}$ KI compared with WT mice (Figure S1F). Analysis of ACKR4$^{GFP/+}$ Het or ACKR4$^{GFP/GFP}$ KI mice by fluorescence stereomicroscopy confirmed ACKR4 expression in LECs of the LN SCS ceiling (Ulvmar et al., 2014) (Figure S1G) and also revealed ACKR4^{GFP} expression in afferent collectors immediately upstream of the LN (Figures S1G and S1H), as well as in larger efferent collectors, such as the flank collector (Figure S1I). Strong ACKR4^{GFP} expression was also detected by confocal microscopy of efferent flank collectors (Figure 1D). In the upper skin, ACKR4^{GFP} was broadly expressed in epidermal keratinocytes and hair follicles (Figures 1E and S1J), whereas LYVE-1^{+} lymphatic capillaries were devoid of ACKR4^{GFP} expression (Figure 1E). Similarly, lymphatic capillaries in the diaphragm were negative for ACKR4^{GFP} (Figure S1K). In agreement with our RNA sequencing analyses (Figures 1B and 1C), we identified a subset of dermal LYVE-1^{-} lymphatic collectors that expressed the ACKR4^{GFP} (Figure 1F). Intriguingly, the switch from ACKR4^{GFP}-expressing to non-expressing segments often occurred at a valve or a vessel branching point (Figure 1F). By contrast, the majority of mesenteric lymphatic vessels, which are mainly collectors, expressed ACKR4^{GFP} (Figure 1G). When investigating mesenteric lymphatics in more detail, it became evident that the first few vessel branches exiting the intestine typically were ACKR4^{GFP} negative, while the more downstream vessel segments, in closer proximity to the draining mesenteric LNs, were all ACKR4^{GFP} positive (Figure 1H). In conclusion, our analysis revealed that ACKR4^{GFP} expression was limited to a subset of afferent lymphatic collectors.

ACKR4 expression correlates with smooth muscle cell coverage of dermal lymphatic collectors

Large lymphatic collectors display a dense LMC coverage, which mediates lymph propulsion (von der Weid and Zawieja, 2004). Since ACKR4 expression appeared to be a characteristic feature of afferent collectors located further downstream in the lymphatic vessel tree (Figures 1G and 1H), we next investigated whether ACKR4 expression correlated with the presence of α-smooth muscle actin (SMA)$^{+}$ LMCs. When we co-stained dorsal ear skin halves of ACKR4$^{GFP/GFP}$ KI and ACKR4$^{GFP/+}$ Het mice for CD31 and SMA, we found that the network of SMA^{+} cells indeed was significantly higher around ACKR4^{GFP}-positive compared with ACKR4^{GFP}-negative collecting vessel segments (Figures 1I–1K). No difference in SMA density was observed between ACKR4$^{GFP/GFP}$ KI and ACKR4$^{GFP/+}$ Het mice (Figures 1J and 1K), indicating that loss of ACKR4 expression had no direct impact on the SMA^{+} LMC coverage.

Lack of ACKR4 expression does not impact lymphatic morphology and function

To investigate if lymphatic morphology and drainage function were altered in the absence of ACKR4, we measured lymphatic drainage from the ear skin and analyzed collector morphology in the mesentery of ACKR4$^{GFP/GFP}$ KI and ACKR4$^{GFP/+}$ Het mice. Analysis of PROX1^{+} vasculature in mesenteries revealed no difference in the organization of the lymphatic network (Figures S2A and S2B). Similarly, we observed no differences in lymphatic drainage between ACKR4$^{GFP/GFP}$ KI and WT mice, neither in steady state nor in skin inflammation induced by topical application of the phorbol ester 12-O-tetradecanoylphorbol-13-acetate (TPA) (Figures S2C–S2F). Thus, global loss of ACKR4 affected neither lymphatic morphology nor drainage function.

ACKR4-expressing LECs bind and take up CCL19 and CCL21

We next performed an *in vivo* chemokine uptake assay to investigate whether dermal collectors expressed functional ACKR4. For this we harvested split ear skin halves of ACKR4$^{GFP/GFP}$ KI and ACKR4$^{GFP/+}$ Het mice and incubated them for 1 h at 37°C with fluorescent CCL19 (CCL19-AF647) and anti-CD31-PE antibody. GFP-expressing collectors of ACKR4$^{GFP/+}$ Het mice bound significantly more CCL19-AF647 than those of ACKR4$^{GFP/GFP}$ KI mice (Figures 2A and 2B). To address whether CCL19 was taken up or solely presented on ACKR4 on the cell surface, we co-incubated split ear skin halves with CCL19-AF647 and LysoTracker, which stains lysosomes. Although, not all CCL19-AF647^{+} spots co-localized with LysoTracker, we could indeed identify double-positive vesicles in collector LECs of ACKR4$^{GFP/+}$ Het mice (Figures S3A–S3C). We next co-injected CCL19-AF647 and anti-CD31-PE antibody subcutaneously into the paw of ACKR4$^{GFP/GFP}$ KI mice and ACKR4$^{GFP/+}$ Het mice and harvested the draining leg collector 30 min later for confocal analysis. The CD31-PE signal intensity was used

Figure 2. ACKR4-expressing LECs bind and take up CCL19 and CCL21

(A and B) Ear skin explants of ACKR4$^{GFP/GFP}$ KI and ACKR4$^{GFP/+}$ Het mice were incubated at 37°C with CCL19-AF647 and CD31-PE, and GFP^{+} collectors were analyzed by confocal microscopy 1 h later. (A) Representative images of ACKR4$^{GFP/GFP}$ KI (bottom) and ACKR4$^{GFP/+}$ Het (top). Scale bars, 50 μm. (B) Left: mean intensity of CCL19-AF647 from one out of two similar experiments with three to six images from one mouse. Mean ± SEM, Student's t test. Right: summary of the two different experiments (each connected by a line).

(C–F) ACKR4$^{GFP/GFP}$ KI and ACKR4$^{GFP/+}$ Het mice were subcutaneously co-injected into the hind paw with either (C and D) CCL19-AF647 or (E and F) CCL21-Dy649 and anti-CD31-PE. Leg collectors were dissected and analyzed by confocal microscopy after 30 min. (C and E) Representative images of ACKR4$^{GFP/+}$ Het mice (top) and ACKR4$^{GFP/GFP}$ KI mice (bottom). Higher optical magnification images of the CCL21-Dy649 signal (right). Scale bars, 50 μm. (D and F) Quantification of the mean intensity of (D, left) CCL19-AF647 and (F, top) CCL21-Dy649 normalized to the mean intensity of CD31-PE from one out of four similar experiments with one mouse per group and four to seven images per condition. Mean ± SEM, Student's t test. (D) Right: CCL19-AF647 and (F) bottom: summary of the different experiments performed (each connected by a line).

(G–I) A CCL21-Dy549 uptake assay was performed in human dermal LECs transfected with plasmid driving expression of either ACKR4-GFP or ACKR3-GFP, or with a vehicle control at either 37°C or on ice. Top row: representative histogram plots. Bottom row: summary of the mean fluorescence intensities (MFI) measured in four independent experiments. Mean, paired Student's t test.

for normalizing the CCL19-AF647 signal, to account for varying tissue depth of the collecting vessels. This analysis revealed a strong signal for CCL19-AF647 in GFP-expressing collector segments of ACKR4$^{GFP/+}$ Het mice but not in ACKR4$^{GFP/GFP}$ KI mice (Figures 2C and 2D). We next repeated the leg collector uptake assay with fluorescently labeled CCL21 (CCL21-Dy649), which, however, is less suited for probing ACKR4 function, since it readily adheres to negatively charged cell surfaces and matrix components due to its positively charged C terminus (Artinger et al., 2021). Despite of its intrinsic stickiness, CCL21-Dy649 strongly co-localized with GFP$^+$ collecting vessels in ACKR4$^{GFP/+}$ Het mice and less in ACKR4$^{GFP/GFP}$ KI mice (Figures 2E and 2F). In ACKR4$^{GFP/+}$ Het mice, CCL21-Dy649 displayed a granular staining pattern, indicative of cellular uptake into LECs, which was largely absent in ACKR4$^{GFP/GFP}$ KI mice (Figure 2E). To further investigate the CCL21-scavenging function of ACKR4, we performed CCL21-Dy549 uptake assays in cultured human LECs transfected with plasmids encoding a GFP-tagged ACKR4 or ACKR3, respectively. Notably, ACKR3 does not bind CCR7 ligands (Nibbs and Graham, 2013) and served as negative control. LECs transfected with ACKR4-GFP, ACKR3-GFP, or vehicle control (CTR) were incubated for 1 h at 37°C with CCL21-Dy549, subjected to an acidic wash to remove surface-bound chemokine and subsequently analyzed by FACS. The CCL21-Dy549 signal in ACKR4-GFP-transfected LECs was significantly higher than in ACKR3-GFP-transfected LECs (Figures 2G and S3D). Moreover, the CCL21-Dy549 signal in ACKR4-GFP-transfected LECs was lost when the uptake experiment had been performed on ice, i.e., a temperature at which cellular internalization processes are blocked (Figures 2H and 2I). Taken together, these results confirmed that ACKR4 functions as a scavenger of both CCR7 ligands in lymphatic collectors.

ACKR4 expression is induced by flow

Since we found ACKR4 to be most prominently expressed in lymphatic collectors with higher LMC coverage, we hypothesized that ACKR4 expression might be induced by flow. In support of this hypothesis, we had previously observed in a microarray transcriptomics study that ACKR4 was upregulated in cultured human intestinal LECs in response to laminar flow (Sabine et al., 2015), and we confirmed this observation by qRT-PCR analysis (Figure 3A). To study the flow-dependence of ACKR4 expression in dermal LECs we made use of another *in vitro* flow system, which involved culturing dermal LEC monolayers on an orbital shaker (Salek et al., 2012). While LECs in the well's periphery aligned in the direction of the predominately laminar flow, cells cultured under static conditions kept their characteristic cobble-stone-like morphology (Figure 3B). Also in this model, we observed a flow-induced upregulation of ACKR4 RNA in LECs (Figure 3C). To test ACKR4 functionality, we next performed *in vitro* uptake assays with CCL19-AF647 and CCL21-Dy649 using the same system. In the case of CCL21-Dy649, no difference in fluorescent signal intensity between flow-exposed and static LECs was observed, indicating that the flow-induced upregulation of ACKR4 *in vitro* might have been too subtle to overcome the limitations of the sticky CCL21 chemokine probe (Figure S3E). Conversely, in the case of CCL19-AF647, the fluorescent signal was markedly enhanced in LECs that had been subjected to flow (Figure 3D). When repeating the uptake experiments in flow-exposed LECs on ice, the CCL19-AF647 signal was almost completely lost (Figure 3E), indicating impaired chemokine internalization under these conditions.

ACKR4 expression is lost in Foxc2$^{\Delta LEC}$ mice, which display lymphatic dysfunction

To address the flow-dependence of ACKR4 expression *in vivo*, we analyzed ACKR4 levels in lymphatic collectors in a lymphedema setting, namely in mesenteric collecting vessels of postnatal day 7 Foxc2$^{fl/fl}$xProx1-Cre^{ERT2} mice (Sabine et al., 2015), in which Foxc2 expression had been specifically ablated in LECs (Foxc2$^{\Delta LEC}$ mice). Foxc2 is a transcription factor crucial for both embryonic and postnatal lymphatic development and function (Norrmén et al., 2009; Petrova et al., 2004; Sabine et al., 2015). When Foxc2 is conditionally ablated by tamoxifen injection on postnatal day 4, as in our experiment, valve development in the growing mesentery is abrogated and mice develop chylous ascites, as a result of lymph stasis and leaky lymphatics (Sabine et al., 2015). Staining mesenteric collecting vessels with an ACKR4-specific antibody, ACKR4 was detectable in WT controls but was almost completely lost in Foxc2$^{\Delta LEC}$ mice (Figure 3F). Similarly, when analyzing a single-cell sequencing dataset of capLECs and colLECs derived from mesentery of 6-week-old WT and Foxc2$^{\Delta LEC}$ mice 3 weeks after tamoxifen administration (Gonzalez-Loyola et al., 2021), *Ackr4* expression in colLECs was lost in the absence of *foxc2* (Figure 3G). Collectively, these findings demonstrated that flow-induced ACKR4 expression in LECs *in vitro* and indicated a similar role of flow *in vivo*.

TPA-induced inflammation results in accumulation of CD4$^+$ T cells in ACKR4-deficient collectors

While DCs and T cells actively crawl within lymphatic capillaries, they typically detach from the endothelium in the collectors to be rapidly transported to the dLNs by the lymph flow. Considering that we found ACKR4 to be upregulated by flow in afferent lymphatic collectors, we hypothesized that it might serve to remove CCL21 from the LEC surface (Bao et al., 2010; Russo et al., 2016; Yin et al., 2010) to prevent induction of integrin-mediated firm adhesion of leukocytes in afferent collectors. The latter process is well known to occur in high endothelial venules (HEVs), which also present CCL21 to leukocytes under flow (Stein et al., 2000; Woolf et al., 2007). However, in contrast to HEVs, afferent lymphatics express only minute levels of the integrin ligands ICAM-1 and VCAM-1 in steady state, but upregulate these molecules in inflammation (Arasa et al., 2021; Johnson et al., 2006; Vigl et al., 2011). Thus, we further hypothesized that an overabundance of CCL21 caused by loss of ACKR4 might induce adhesion and consequently lead to a reduced rate of detachment (k_{detach}) and accumulation of migrating leukocytes in lymphatic collectors in the context of inflammation.

Considering that the contribution of ACKR4 to lymphatic trafficking of T cells is completely unknown so far, we decided to focus on this cell type and specifically on antigen-experienced CD4$^+$ T cells, which represent the main T cells migrating through afferent lymphatics (Bromley et al., 2013; Tomura et al., 2010). To analyze the spatial distribution of endogenous CD4$^+$ T cells in dermal

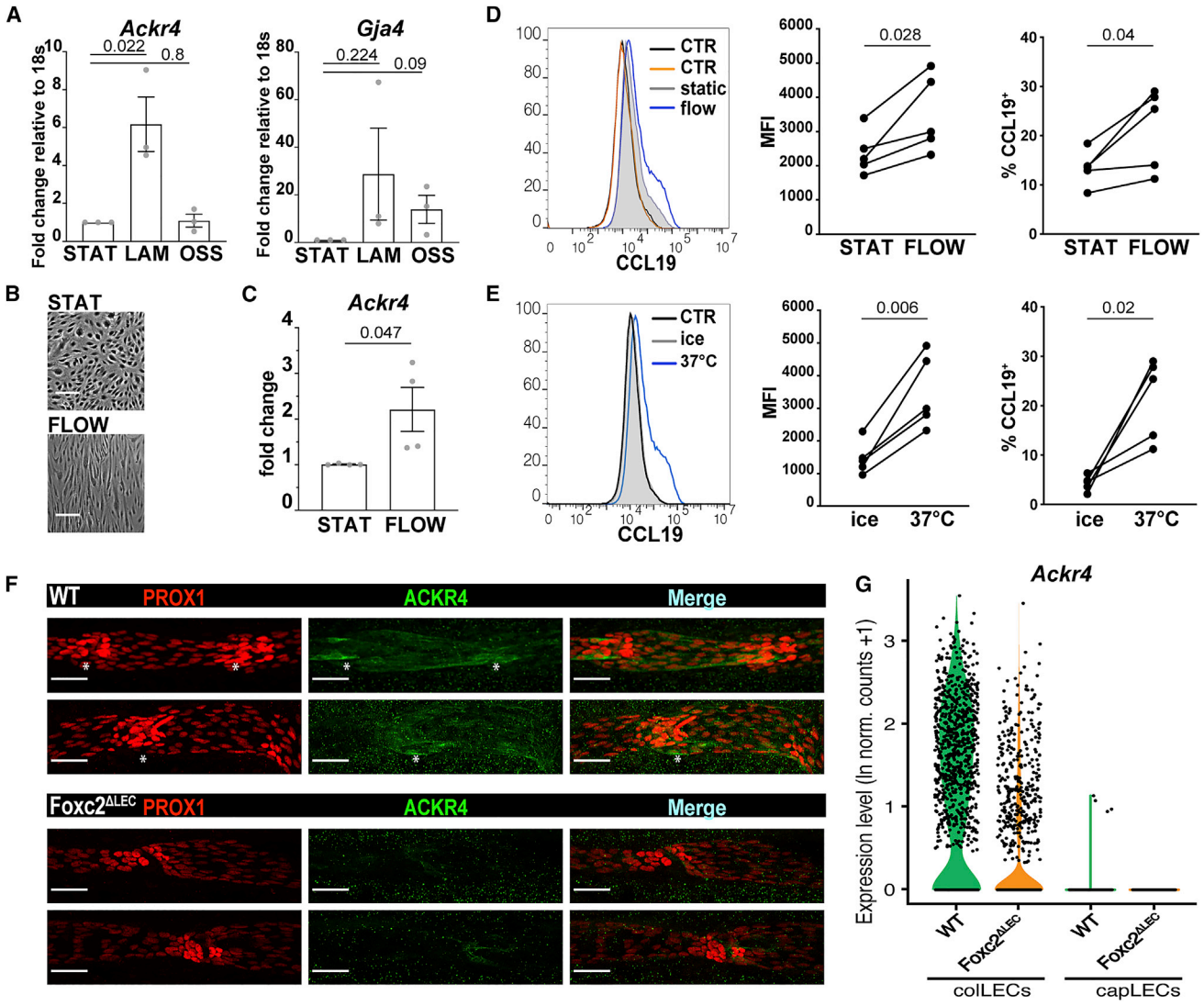

Figure 3. ACKR4 expression is induced by flow

(A) qPCR analysis of *ACKR4* expression in human intestinal LECs after exposure to static conditions (STAT), laminar (LAM), or oscillatory (OSS) flow. Upregulation of flow-induced *Gja4* (connexin37; Sabine et al., 2012) was evaluated as positive control. n = 3 experiments/condition.

(B–E) Human dermal LEC monolayers were subjected to flow on an orbital shaker for 48 h. (B) Representative images, taken in the well periphery, of cells left at static conditions (up) or subjected to flow (down). Scale bars, 200 μm. (C) RNA expression of *ACKR4* in human dermal LECs analyzed by qPCR in four independent experiments (mean ± SEM). (D and E) A CCL19-AF647 uptake assay was performed on human dermal LECs previously subjected to flow or static conditions at either (D) 37°C or (E) comparing uptake by flow-exposed LECs at 37°C or on ice. Left: representative histograms; right: summary of the mean fluorescence intensity (MFI) of CCL19-AF647 and the percentage of CCL19-AF647$^+$ cells. n = 5 experiments per condition (connected by a line).

(F) Confocal images of mesentery collectors stained for ACKR4 expression (green) and PROX1 (red) in WT (up) or FOXC2Δ^{LEC} (down) mice. Scale bars, 50 μm.

(G) Violin plot of Ackr4 gene expression from scRNA-seq data (Gonzalez-Loyola et al., 2021) of mesenteric capLECs and colLECs isolated from WT and FOXC2Δ^{LEC} mice. Statistics: unpaired Student's t test (A and C), mean ± SEM. Paired Student's t test (D and E).

lymphatic capillaries and collectors, we performed quantitative whole-mount analyses in steady-state ear skin of ACKR4$^{GFP/GFP}$ KI and ACKR4$^{GFP/+}$ Het mice. After staining for CD31, CD4, and CD45 we acquired confocal images of CD31$^+$ capillaries, identified by their characteristic morphology, and of CD31$^+$ ACKR4^{GFP} collectors, and performed a blinded analysis of CD4$^+$CD45$^+$ T cells co-localizing with either vessel type. Loss of ACKR4 did not lead to major differences in CD4$^+$CD45$^+$ T cell co-localization with capillaries in steady-state ear skin (Figures S4A–S4E), indicating that, in contrast to DCs (Bastow et al., 2021), CD4$^+$ T cell recruitment from the tissue toward and into lymphatics was not impaired. When analyzing CD31$^+$GFP$^+$ collecting vessel segments (Figures 4A and 4B) we observed that the average GFP$^+$ vessel length was slightly higher in ACKR4$^{GFP/GFP}$ KI compared with ACKR4$^{GFP/+}$ Het mice (Figure 4C), likely because of stronger GFP expression in ACKR4$^{GFP/GFP}$ KI mice. In contrast to capillaries, virtually no CD4$^+$ T cells were found within lymphatic collectors in steady state (Figures 4D and 4E). In fact, in 86% and 95% of

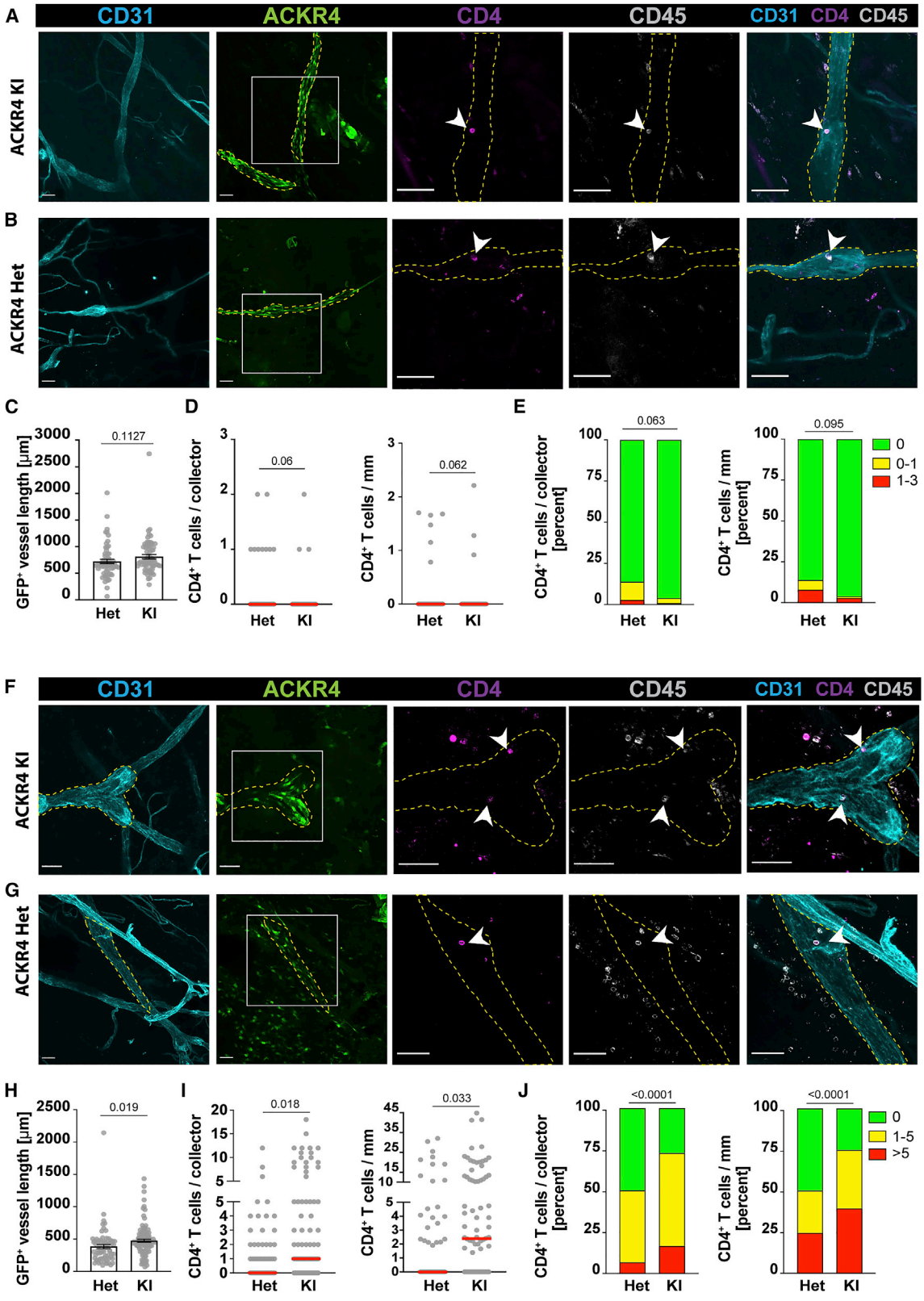

(legend on next page)

all images of ACKR4$^{GFP/+}$ Het mice and ACKR4$^{GFP/GFP}$ KI mice analyzed, no T cells were detected (Figure 4E), and in the remaining images only one to two cells were detected. Although more collectors with one to three cells were captured in the ACKR4$^{GFP/+}$ Het mice, these differences remained minute, due to the extremely low cell counts (Figures 4D and 4E).

We next repeated the whole-mount analysis under inflammatory conditions, namely 16 h after topically treating ears with TPA (Figure S5A). TPA treatment induced a similar ear swelling response and leukocyte recruitment in both genotypes (Figures S5C and S5D). No major differences between CD4$^+$ T cell numbers co-localizing with inflamed capillaries of ACKR4$^{GFP/+}$ Het mice and ACKR4$^{GFP/GFP}$ KI mice were observed (Figures S4F–S4J), indicating no impairment in T cell recruitment from the tissue into lymphatic capillaries in TPA-induced inflammation. In comparison to steady-state conditions (Figures 4D and 4E), strikingly more CD4$^+$ T cells were detected in inflamed collectors (Figures 4I and 4J). Moreover, we observed a significant increase in CD4$^+$ T cells co-localizing with GFP$^+$ collecting vessel segments of ACKR4$^{GFP/GFP}$ KI compared with ACKR4$^{GFP/+}$ Het mice in TPA-induced inflammation (Figures 4I and 4J). Overall, these data confirmed that, in the absence of ACKR4 expression, endogenous T cells accumulated in TPA-inflamed collectors but not in capillaries, indicating that—in line with our hypothesis—their detachment rate in collectors was reduced.

In the absence of ACKR4, short-term migration of Kik^{red} CD4$^+$ T cells from photoconverted steady-state skin to dLNs is reduced

The fact that we found T cells accumulating in TPA-inflamed lymphatic collectors of ACKR4$^{GFP/GFP}$ KI mice suggested that their migration from inflamed skin to dLNs might be compromised. To investigate whether ACKR4 indeed supports lymphatic migration of endogenous T cells in inflammation, we crossed ACKR4$^{GFP/GFP}$ KI mice with mice expressing the photoconvertible fluorescent protein Kikume Green-Red (KikGR) in all cell types (Tomura et al., 2014). In KikGR mice, the KikGR protein is converted from Kik^{green} to Kik^{red} upon exposure to violet light. Thus, migratory leukocytes photoconverted in the skin can subsequently be identified as Kik^{red} cells in dLNs (Tomura et al., 2014). Notably, photoconversion of Kik^{green} to Kik^{red} cells is expected to occur in the entire skin, including cells already present within the lymphatic capillaries and collectors. To specifically investigate the behavior of intralymphatic T cells, we decided to illuminate the skin and harvest the skin-draining LNs already 6 h after photoconversion (Figure 5A), i.e., at a time point considered too short for DCs or T cells to migrate all the way from the tissue via capillaries and collectors to dLNs (Kissenpfennig et al., 2005; Tomura et al., 2014). Therefore, the number of T cells or DCs arriving in the dLN in such a short-term photoconversion experiment should primarily depend on the number of cells present in collectors—and possibly also in upstream capillaries—at the time of photoconversion and on the rate at which these cells detach in collectors (k_{detach}).

Interestingly, we observed that the photoconversion procedure itself already induced a mild inflammatory response, as demonstrated by a significant increase in neutrophils in the illuminated skin and in dLNs at the 6 h time point (Figures 5A–5C, S5E, and S5F). When analyzing the number of Kik^{red} T cells in dLNs 6 h after photoconversion of steady-state belly skin (Figure 5A), we found a slight reduction in the numbers and percentages of CD4$^+$ Kik^{red} cells and CD8$^+$ Kik^{red} cells in KikGRxACKR4$^{GFP/GFP}$ KI mice (Figures 5D, 5E, and S6A), which might have been caused by retention of T cells in upstream collectors caused by TPA-induced inflammation. In contrast, reduced leukocyte arrival was significantly more profound for Kik^{red} migratory DCs (Figure 5F), which in the absence of ACKR4 reportedly already display a defect in entry into lymphatic capillaries (Bastow et al., 2021).

In the absence of ACKR4, short-term migration of Kik^{red} CD4$^+$ T cells from photoconverted TPA-inflamed skin to dLNs is enhanced

We next repeated our short-term photoconversion experiments in inflamed skin. In analogy to the conditions used for the whole-mount analyses (Figures 4 and S4), the ear skin of KikGRxACKR4$^{GFP/GFP}$ KI and KikGRxACKR4$^{+/+}$ WT mice was inflamed by topical administration of TPA and photoconverted 16 h later (Figure 5G). When analyzing cell migration 6 h after photoconversion, the percentage and number of CD4$^+$ Kik^{red} cells in dLNs of KikGRxACKR4$^{GFP/GFP}$ KI compared with KikGRxACKR4$^{+/+}$ WT mice were significantly increased (Figures 5H and S6A), indicating that the striking increase in cells present in ACKR4-deficient collectors at the time point of photoconversion (Figures 4I and 4J) had compensated for the reduced rate of detachment (k_{detach}). Notably, CD8$^+$ Kik^{red} cells and Kik^{red} migratory DCs were not increased (Figures 5I and 5J), indicating that they had not been accumulating in ACKR4-deficient collectors at the time point of photoconversion.

Migration of adoptively transferred T cells to dLNs is reduced in ACKR4$^{GFP/GFP}$ KI mice

Finally, to validate the observed migration phenotype in another model, we performed adoptive transfer experiments. In a first

Figure 4. CD4$^+$ T cells accumulate in lymphatic collectors of ACKR4$^{GFP/GFP}$ KI mice in TPA-induced inflammation

Whole mounts prepared from (A–E) steady-state or (F–J) TPA-inflamed ear skin of ACKR4$^{GFP/+}$ Het and ACKR4$^{GFP/GFP}$ KI mice were stained for CD31, CD45, and CD4. Confocal images were acquired. For the quantification of CD45$^+$CD4$^+$ T cells in collectors, a region of interest (ROI) was placed over CD31$^+$ ACKR4^{GFP}-positive collectors and the number of CD45$^+$CD4$^+$ T cells within the ROI was quantified. Representative images of intralymphatic CD4$^+$ T cells in whole mounts prepared from (A and B) steady-state or (F and G) TPA-inflamed ear skin of either genotype. White arrows indicate CD4$^+$CD45$^+$ T cells. Scale bars, 50 μm (in all images). (C and H) Analysis of the ACKR4^{GFP}-positive collector vessel length/ROI. (D and I) Quantification of CD4$^+$ T cells. Left: per ROI; right: per mm of GFP$^+$ collector vessel. (E and J) Distribution analysis comparing the frequencies of images with 0 cells, 0–1 cells, and 1–3 cells in (E), and 0 cells, 1–5 cells and >5 cells in (J). Left: per ROI; right: normalized to mm of GFP$^+$ collector vessel. Images (ROIs) from 9 mice/group were analyzed in (C–E) and from 6–7 in (H–J). Each dot in (C, D, H, and I) represents the value from one ROI. Analysis in (C–E): n = 61 for the Het and 68 for the KI group, analysis in (H–J): n = 69 for the Het and 102 for the KI group. Medians are shown in red, means in black. (C and H) Student's t test, (D, E, I, and J) Mann-Whitney test, (E and J) chi-square distribution analysis.

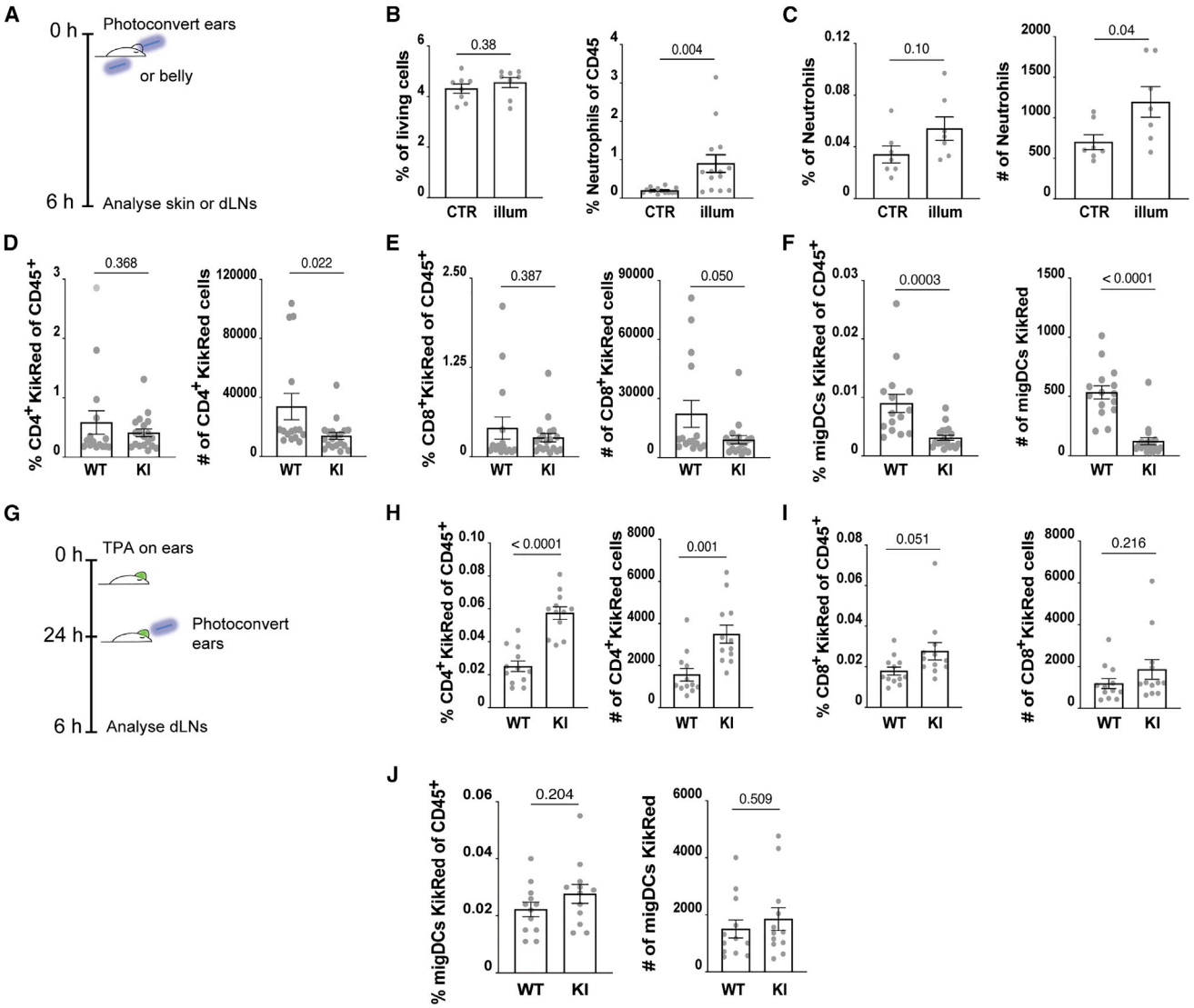

Figure 5. ACKR4 modulates short-term migration of photoconverted CD4⁺ T cells through afferent collectors in TPA-induced inflammation

(A–C) Photoconversion induces a mild inflammatory response in the illuminated skin. (A) Steady-state skin was illuminated for photoconversion (illum) or left untreated (CTR) and analyzed 6 h later. (B) Quantification of the percentages of $CD45^+$ cells and of $CD11b^+Ly\text{-}6G^+$ neutrophils in photoconverted ear skin, and (C) percentages and absolute numbers of neutrophils in ear skin-dLNs.

(D–F) Belly skin of $KikGRxACKR4^{GFP/GFP}$ (KI) and $KikGRxACKR4^{+/+}$ (WT) mice was photoconverted as in (A) and pooled dLNs analyzed by FACS after 6 h. Quantification of (D) $CD4^+$ Kik^{red} cells, (E) $CD8^+$ Kik^{red} cells, and (F) $Kik^{red}CD11c^+$ $MHCII^{high}$.

(G–J) TPA-inflamed ears of $KikGRxACKR4^{GFP/GFP}$ (KI) and $KikGRxACKR4^{+/+}$ (WT) mice were photoconverted and pooled dLNs analyzed by FACS after 6 h. (G) Depiction of the experiment. Quantification of (H) $CD4^+$ Kik^{red} cells, (I) $CD8^+$ Kik^{red} cells, and (J) $Kik^{red}CD11c^+$ $MHCII^{high}$. Mean ± SEM from two to three pooled experiments are shown in (A and C), (D and F), (G–I). One dot represents one mouse. Student's t test.

approach, we adoptively transferred lymphocytes expressing dsRed in all T cells(Veiga-Fernandes et al., 2007) into the steady-state footpads of $ACKR4^{GFP/GFP}$ KI and WT mice and analyzed the dLNs 16 h later. Significantly fewer $dsRed^+CD4^+$ and $dsRed^+CD8^+$ T cells were detected in dLNs of $ACKR4^{GFP/GFP}$ KI compared with WT mice (Figures 6A, 6B, 6C, and S6B). When analyzing the localization of adoptively transferred T cells in popliteal LN sections by confocal microscopy, we found that—in contrast to DCs (Ulvmar et al., 2014)—T cells that made it to the LN did not accumulate in the LN SCS, but were able to enter the LN parenchyma of $ACKR4^{GFP/GFP}$ KI mice (Figures S7A and S7B). Furthermore, we performed a similar adoptive transfer experiment, but this time transferring lymphocytes from KikGR mice into TPA-inflamed ear skin. Eighteen hours later, significantly fewer $Kik^{green}CD4^+$ and $Kik^{green}CD8^+$ T cells were detected in ear-draining LNs of $ACKR4^{GFP/GFP}$ KI compared with WT mice (Figures 6D, 6E, 6F, and S6B). Overall, these findings confirmed that, in the absence of ACKR4, migration of adoptively transferred T cells from skin to dLNs was compromised.

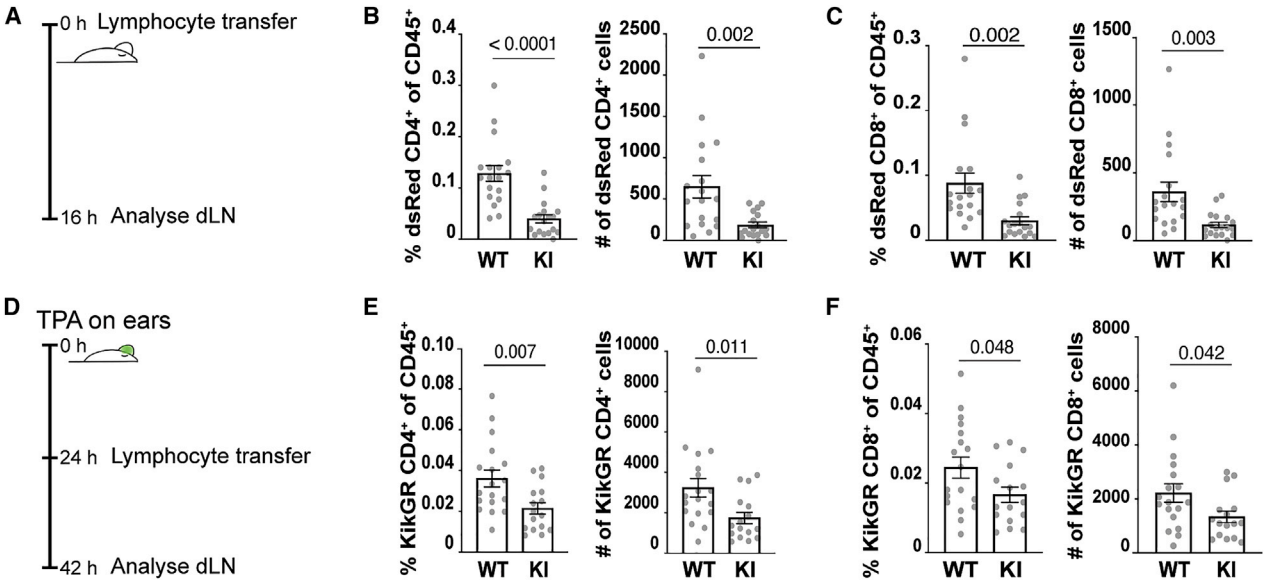

Figure 6. In the absence of ACKR4 lymphatic migration of T cells transferred into steady-state or TPA-inflamed skin is reduced

(A–C) dsRed^{+} lymphocytes were adoptively transferred into steady-state footpads of ACKR4$^{GFP/GFP}$ KI and WT mice and dLNs analyzed 16 h later. (A) Schematic depiction of the experiment. (B and C) Analysis of the percentage and total numbers of (B) dsRed^{+}CD4^{+} and (C) dsRed^{+}CD8^{+} T cells.

(D–F) Kik^{green} lymphocytes were adoptively transferred into TPA-inflamed ears of ACKR4$^{GFP/GFP}$ KI and WT mice and dLNs analyzed 18 h later. (D) Schematic depiction of the experiment. (E and F) Analysis of the percentage and total numbers of (E) Kik^{green}CD4^{+} and (F) Kik^{green}CD8^{+} T cells. Mean ± SEM from three pooled experiments are shown in (B and C) and (E and F). One dot represents one mouse. Student's t test.

DISCUSSION

While previous studies have identified a contribution of ACKR4 to DC chemotaxis in the context of lymphatic migration (Bastow et al., 2021; Bryce et al., 2016; Ulvmar et al., 2014), we here describe an additional role of ACKR4 in scavenging and removing chemokine from the endothelial surface within lymphatic collectors, to facilitate T cell de-adhesion and rapid, passive transport with the lymph flow to dLNs. Antigen-experienced T cells, in particular CD4^{+} effector-memory cells and regulatory T cells, are the most abundant cell types migrating through afferent lymphatics (Bromley et al., 2013; Tomura et al., 2010), but their migration is less well studied compared with the one of DCs. Recirculation of T cells, which occurs constantly and at an enhanced rate during inflammatory conditions, is considered important for immunosurveillance, maintenance of tolerance, and dampening of inflammatory responses in peripheral tissues (Collado-Diaz et al., 2021; Permanyer et al., 2018). By contributing to de-adhesion of T cells in afferent collectors in inflammation, ACKR4 is therefore expected to affect tissue exit and recirculation of T cells and, as such, contribute to the regulation of T cell-mediated immunity.

In contrast to leukocyte transport in blood, leukocyte movement in afferent lymphatics relies in part on active cell migration. Upon entry into lymphatic capillaries, DCs and T cells need to first actively crawl to reach downstream lymphatic collectors, where lymph flow is strongly increased due to contractions of the collector-surrounding LMCs. Only in this compartment do leukocytes de-adhere and are rapidly transported to dLNs with the flow (Collado-Diaz et al., 2021). Induction of ACKR4 expression by flow fits well with the description here of its role in promoting T cell de-adhesion in dermal collectors. ACKR4 induction by flow was observed in our cell-based *in vitro* assays and also suggested by the near-complete absence of ACKR4 in mesenteric collectors of FOXC2Δ^{LEC} mice, which display defective lymph transport (Sabine et al., 2015). In further support of our findings, a computational simulation of flow patterns in LNs recently showed that shear stress was higher on LECs forming the SCS ceiling, which express ACKR4 (Ulvmar et al., 2014), compared with LECs forming the SCS floor, which lack ACKR4 expression (Jafarnejad et al., 2017).

Our microscopy-based analyses indicated that T cell entry into lymphatic capillaries was not affected by the absence of ACKR4, neither in steady state nor in TPA-induced inflammation. This is in contrast to the reported function of ACKR4 in DC migration into afferent lymphatics (Bastow et al., 2021; Bryce et al., 2016). Similarly, we and others observed that entry of T cells from the SCS into the LN parenchyma, was not or only marginally compromised upon loss of ACKR4 (Figures S7A and S7B) (Martens et al., 2020). This is in contrast to the essential role of ACKR4 in DC emigration from the SCS (Ulvmar et al., 2014). A possible explanation for this difference in the ACKR4 dependence might be that activated DCs, but not T cells, produce CCL19 (Bruckner et al., 2012; Luther et al., 2000; Ngo et al., 1998b; Sallusto et al., 1999b). This difference might render DCs more dependent on ACKR4-mediated scavenging of CCL19 and CCL21, first during entry into afferent lymphatics (Bryce et al., 2016) and later on when exiting the SCS.

The only location where loss of ACKR4 had a dramatic impact on the distribution of endogenous CD4^{+} T cells was at the level

of the TPA-inflamed dermal lymphatic collectors; here we found strikingly more endogenous $CD4^+$ T cells accumulating in $ACKR4^{GFP/GPF}$ KI compared with $ACKR4^{GFP/+}$ Het mice. Our 6 h photoconversion experiments revealed that, in the absence of ACKR4, less photoconverted T cells were present in dLNs when photoconversion had occurred in steady-state skin, whereas more T cells were present upon converting TPA-inflamed skin. Considering that our whole-mount quantifications detected no reduction in T cells in steady-state capillaries and virtually no T cells present in steady-state collectors (Figures 4 and S4), the reduction observed in the steady-state photoconversion experiments was likely caused by the illumination-induced tissue inflammation, leading to the arrest of T cells arriving from capillaries in ACKR4-deficient collectors. Conversely, when photoconverting TPA-inflamed skin, where at this time point a lot of T cells were already accumulating in ACKR4-deficient collectors (Figures 4I and 4J), significantly more cells got converted in this compartment in the absence of ACKR4, resulting in an overall increase in photoconverted $CD4^+$ T cells found in dLNs after 6 h. Why this effect was more pronounced in $CD4^+$ than in $CD8^+$ T cells is presently not clear, but could, e.g., be due to differences in T cell recirculation kinetics, CCR7 signaling or expression levels, or contribution of additional chemokine receptors to lymphatic trafficking (Britschgi et al., 2008; Gerlach et al., 2016). Interestingly, in our photoconversion experiments, ACKR4 deficiency led to a significant reduction in photoconverted DCs in dLNs upon illuminating steady-state skin, whereas equal numbers of DCs were present in dLNs upon illuminating TPA-inflamed skin. The reduction in DC migration to dLNs observed in steady state is likely caused by the previously reported entry defect into afferent lymphatics in the absence of ACKR4 (Bastow et al., 2021), resulting in fewer intralymphatic DCs that got photoconverted within lymphatics under steady-state conditions. Conversely, the fact that no difference in DC numbers in dLNs was observed when repeating the 6 h photoconversion experiment in TPA-inflamed skin suggests that, under inflammatory conditions, also DCs might be retained in ACKR4-deficient collectors, and that this effect, which leads to an enhanced photoconversion rate, compensated for the defective lymphatic entry caused by ACKR4 deficiency.

Our conclusion that ACKR4 facilitates T cell exit from tissues by promoting de-adhesion in inflamed collectors is further supported by our adoptive transfer experiments: lymphocyte transfer into either TPA-inflamed or steady-state skin resulted in a significant reduction in $CD4^+$ and $CD8^+$ T cells retrieved from the dLNs 16–18 h later. We suspect that the reduction observed upon transfer into steady-state skin is caused by inflammatory events triggered by the cell injection (e.g., death of transferred cells), leading to upregulation of adhesion molecules in lymphatic collectors. According to the paradigm of lymphatic trafficking, leukocyte entry is thought to primarily occur at the level of capillaries (Collado-Diaz et al., 2021; Permanyer et al., 2018). However, we have recently reported that, in the context of tissue inflammation, DCs additionally enter in a CCR7/CCL21- and β1 integrin/VCAM-1-dependent manner into dermal lymphatic collectors (Arasa et al., 2021). It is possible that also T cells, which require the same molecules for lymphatic migration (Bromley et al., 2013; Teijeira et al., 2017), can migrate via this route. Although loss of ACKR4 in collectors could be expected to enhance CCR7-mediated T cell chemotaxis and entry into collectors, we found that overall migration of adoptively transferred T cells to dLNs was reduced, suggesting that intravascular de-adhesion in collectors remained the rate-limiting step modulated by ACKR4 deficiency.

Our data indicate that ACKR4 primarily affects lymphatic migration of T cells by supporting de-adhesion in afferent lymphatic collectors. However, we suspect that ACKR4 might affect further steps in T cell migration. Curiously, when performing photoconversion experiments in steady-state skin and only analyzing photoconverted cell 18 h later, we observed a significant accumulation of Kik^{red} $CD4^+$ T cells in dLNs of ACKR4-deficient mice (Figures S7C–S7G), whereas DC migration remained similarly reduced as at the 6 h time point. One further confounding factor in such a long-term migration experiment is the dwell time of T cells in dLNs: while DCs do not migrate further than the first dLN, tissue-exiting memory T cells are known to continue recirculating through subsequent LNs, blood, and peripheral tissues (Bromley et al., 2013). Of interest in this context could be that CCR7 signaling was shown to promote T cell retention in LNs (Pham et al., 2008). Whether LN exit and T cell recirculation are also affected by ACKR4 is presently unknown.

During T cell homing to LNs through HEVs, CCL21 signaling is known to induce firm arrest of T cells in the vasculature by activating LFA-1 binding to ICAM-1 (Stein et al., 2000; von Andrian and Mackay, 2000; Woolf et al., 2007). While uninflamed lymphatic vessels only express low levels of the integrin ligands VCAM-1 and ICAM-1, both adhesion molecules are upregulated in lymphatic capillaries and collectors in inflammation induced by different stimuli, including TPA (Arasa et al., 2021; Johnson et al., 2006; Teijeira et al., 2017; Vigl et al., 2011). Both ICAM-1 and VCAM-1 were shown to be important for T cell migration from skin to dLNs (Teijeira et al., 2017), and the corresponding integrins LFA-1 and VLA-4 are highly expressed by skin-homing T cells (Schon et al., 2003). Thus, it is likely that these integrin ligands contribute to T cell adhesion in TPA-inflamed collectors. Overall, our study provides evidence that active molecular mechanisms are in place within a defined segment of the lymphatic vasculature during inflammation, to "lubricate" the lining and thus prevent lymphocyte adhesion, allowing intraluminal lymphocytes to undergo an efficient transition from crawling to being passively carried by the lymph flow. Thus, curiously, the sequential steps of lymphocyte-endothelial cell interactions occurring in inflamed lymphatic collectors seem to recapitulate, albeit in a reverse order, the well-described multistep adhesion cascade in blood vessels (Nourshargh and Alon, 2014).

Limitations of the study

A major limitation of our study is that our findings have thus far primarily been made in one inflammatory model, namely, dermal inflammation induced by topical application of TPA. We therefore cannot exclude that the retention of migratory T cells in afferent collectors lacking ACKR4 is dependent on the type of inflammation induced, as the latter might affect expression of integrin ligands, chemokines, and of ACKR4 itself. Furthermore, lymphatic vessels display great heterogeneity in different tissues (Petrova and Koh, 2018). While our study found a migration phenotype cause by ACKR4 deficiency in dermal collectors, it

remains unknown whether ACKR4 exerts the same vessel-lubricating function in afferent lymphatic collectors in other organs or even in large collectors upstream and downstream of LNs, where flow conditions and gene expression will likely be different. Finally, we presently do not know about the human relevance of our findings, since our work was primarily conducted in mice or with human LECs cultures *in vitro*.

STAR★METHODS

Detailed methods are provided in the online version of this paper and include the following:

- KEY RESOURCES TABLE
- RESOURCE AVAILABILITY
  - Lead contact
  - Materials availability
  - Data and code availability
- EXPERIMENTAL MODEL AND SUBJECT DETAILS
  - Mice
  - Human lymphatic endothelial cell culture
- METHOD DETAILS
  - TPA-induced inflammation
  - Adoptive transfer of T cells in steady-state footpads
  - Adoptive transfer of T cells into TPA-inflamed ears
  - CCL21 protein determination in mouse serum
  - Lymphatic drainage assay
  - Whole mount immunofluorescence staining
  - Adoptive transfer of e670 labelled T cells for section staining
  - Chemokine production
  - *Ex vivo* chemokine uptake assay
  - Analysis of SMA coverage
  - Analysis of T cell distribution within lymphatics by microscopy and FIJI (ImageJ)
  - Analysis of T cell migration in KikGRxACKR4^{GFP} mice by FACS
  - OCT sections and immunofluorescence of mouse ear skin sections
  - *In vivo* chemokine uptake assay
  - FACS analysis of TPA-inflamed ears
  - *In vitro* flow experiments
  - *In vitro* chemokine uptake experiments in transfected LECs cell transfection experiments
  - *In vitro* chemokine uptake in flow-exposed LECs
  - Gene expression analysis of in vitro-cultured human LECs
  - Stereomicroscopic analysis of GFP expression
- QUANTIFICATION AND STATISTICAL ANALYSIS

SUPPLEMENTAL INFORMATION

Supplemental information can be found online at https://doi.org/10.1016/j.celrep.2022.110334.

ACKNOWLEDGMENTS

The authors acknowledge support of the Scientific Center for Optical and Electron Microscopy (ScopeM) of ETH Zurich and thank the staff of the ETH Rodent Center HCI and ETH Phenomics Center for animal husbandry. Moreover, we thank Michael Detmar (ETH Zurich) and Marcus Thelen (IRB, Bellinzona, Switzerland) for helpful discussions, Simone Haener and Greta Durini (ETH Zurich) for technical assistance, and Viola Vogel, Andreia Fernandes (ETH Zurich), and Tania Wyss Lozano Hoyos (University of Lausanne) for technical advice. C.H., A.R., and D.F.L. gratefully acknowledge financial support from the Swiss National Fund Sinergia program (CRSII3_160719/1), T.V.P. from the European Union's Horizon 2020 research and innovation program (Theralymph, grant agreement no. 847939), and C.H. additional funding from ETH Zurich.

AUTHOR CONTRIBUTIONS

M.C.F., I.K., and P.S. designed and performed experiments, analyzed data, and edited the manuscript and figures. J.D.M.-S., A.-O.G., A.V., E.C.S., C.S., M.V., C.M., J.A., C.S.D., and E.B. performed experiments and analyzed data. M.T. provided expertise and KikGR mice. A.R., D.F.L., S.T.P., and T.V.P. provided expertise, important reagents, and discussed data. C.H. designed experiments, interpreted data, and wrote the manuscript.

DECLARATION OF INTERESTS

The authors declare no competing interests.

Received: April 26, 2021
Revised: December 2, 2021
Accepted: January 12, 2022
Published: February 1, 2022

REFERENCES

Arasa, J., Collado-Diaz, V., Kritikos, I., Medina-Sanchez, J.D., Friess, M.C., Sigmund, E.C., Schineis, P., Hunter, M.C., Tacconi, C., Paterson, N., et al. (2021). Upregulation of VCAM-1 in lymphatic collectors supports dendritic cell entry and rapid migration to lymph nodes in inflammation. J. Exp. Med. *218*, e20201413.

Artinger, M., Matti, C., Gerken, O.J., Veldkamp, C.T., and Legler, D.F. (2021). A versatile toolkit for semi-automated production of fluorescent chemokines to study CCR7 expression and functions. Int. J. Mol. Sci. *22*, 4158.

Bao, X., Moseman, E.A., Saito, H., Petryniak, B., Thiriot, A., Hatakeyama, S., Ito, Y., Kawashima, H., Yamaguchi, Y., Lowe, J.B., et al. (2010). Endothelial heparan sulfate controls chemokine presentation in recruitment of lymphocytes and dendritic cells to lymph nodes. Immunity *33*, 817–829.

Bastow, C.R., Bunting, M.D., Kara, E.E., McKenzie, D.R., Caon, A., Devi, S., Tolley, L., Mueller, S.N., Frazer, I.H., Harvey, N., et al. (2021). Scavenging of soluble and immobilized CCL21 by ACKR4 regulates peripheral dendritic cell emigration. Proc. Natl. Acad. Sci. U S A *118*, e2025763118.

Braun, A., Worbs, T., Moschovakis, G.L., Halle, S., Hoffmann, K., Bölter, J., Münk, A., and Förster, R. (2011). Afferent lymph-derived T cells and DCs use different chemokine receptor CCR7-dependent routes for entry into the lymph node and intranodal migration. Nat. Immunol. *12*, 879–887.

Britschgi, M.R., Link, A., Lissandrin, T.K.A., and Luther, S.A. (2008). Dynamic modulation of CCR7 expression and function on naive T lymphocytes in vivo. J. Immunol. *181*, 7681–7688.

Bromley, S.K., Thomas, S.Y., and Luster, A.D. (2005). Chemokine receptor CCR7 guides T cell exit from peripheral tissues and entry into afferent lymphatics. Nat. Immunol. *6*, 895–901.

Bromley, S.K., Yan, S., Tomura, M., Kanagawa, O., and Luster, A.D. (2013). Recirculating memory T cells are a unique subset of CD4+ T cells with a distinct phenotype and migratory pattern. J. Immunol. *190*, 970–976.

Bruckner, M., Dickel, D., Singer, E., and Legler, D.F. (2012). Distinct modulation of chemokine expression patterns in human monocyte-derived dendritic cells by prostaglandin E(2). Cell Immunol. *276*, 52–58.

Bryce, S.A., Wilson, R.A.M., Tiplady, E.M., Asquith, D.L., Bromley, S.K., Luster, A.D., Graham, G.J., and Nibbs, R.J.B. (2016). ACKR4 on stromal cells

scavenges CCL19 to enable CCR7-dependent trafficking of APCs from inflamed skin to lymph nodes. J. Immunol. *196*, 3341–3353.

Collado-Diaz, V., Medina-Sanchez, J.D., Gkountidi, A.O., and Halin, C. (2021). Imaging leukocyte migration through afferent lymphatics. Immunol. Rev. https://doi.org/10.1111/imr.13030.

Comerford, I., Nibbs, R.J.B., Litchfield, W., Bunting, M., Harata-Lee, Y., Haylock-Jacobs, S., Forrow, S., Korner, H., and McColl, S.R. (2010). The atypical chemokine receptor CCX-CKR scavenges homeostatic chemokines in circulation and tissues and suppresses Th17 responses. Blood *116*, 4130–4140.

de Paz, J.L., Moseman, E.A., Noti, C., Polito, L., von Andrian, U.H., and Seeberger, P.H. (2007). Profiling heparin-chemokine interactions using synthetic tools. ACS Chem. Biol. *2*, 735–744.

Debes, G.F., Arnold, C.N., Young, A.J., Krautwald, S., Lipp, M., Hay, J.B., and Butcher, E.C. (2005). Chemokine receptor CCR7 required for T lymphocyte exit from peripheral tissues. Nat. Immunol. *6*, 889–894.

Förster, R., Schubel, A., Breitfeld, D., Kremmer, E., Renner-Müller, I., Wolf, E., and Lipp, M. (1999). CCR7 coordinates the primary immune response by establishing functional microenvironments in secondary lymphoid organs. Cell *99*, 23–33.

Gerlach, C., Moseman, E.A., Loughhead, S.M., Alvarez, D., Zwijnenburg, A.J., Waanders, L., Garg, R., de la Torre, J.C., and von Andrian, U.H. (2016). The chemokine receptor CX3CR1 Defines three antigen-experienced CD8 T cell subsets with distinct roles in immune surveillance and homeostasis. Immunity *45*, 1270–1284.

Gonzalez-Loyola, A., Bovay, E., Kim, J., Lozano, T.W., Sabine, A., Renevey, F., Arroz-Madeira, S., Rapin, A., Wypych, T.P., Rota, G., et al. (2021). FOXC2 controls adult lymphatic endothelial specialization, function, and gut lymphatic barrier preventing multiorgan failure. Sci. Adv. *7*, eabf4335.

Gonzalez-Loyola, A., and Petrova, T.V. (2021). Development and aging of the lymphatic vascular system. Adv. Drug Deliv. Rev. *169*, 63–78.

Gosling, J., Dairaghi, D.J., Wang, Y., Hanley, M., Talbot, D., Miao, Z., and Schall, T.J. (2000). Cutting edge: identification of a novel chemokine receptor that binds dendritic cell- and T cell-active chemokines including ELC, SLC, and TECK. J. Immunol. *164*, 2851–2856.

Heinzel, K., Benz, C., and Bleul, C.C. (2007). A silent chemokine receptor regulates steady-state leukocyte homing in vivo. Proc. Natl. Acad. Sci. U S A *104*, 8421–8426.

Hirose, J., Kawashima, H., Swope Willis, M., Springer, T.A., Hasegawa, H., Yoshie, O., and Miyasaka, M. (2002). Chondroitin sulfate B exerts its inhibitory effect on secondary lymphoid tissue chemokine (SLC) by binding to the C-terminus of SLC. Biochim. Biophys. Acta *1571*, 219–224.

Jafarnejad, M., Zawieja, D.C., Brook, B.S., Nibbs, R.J.B., and Moore, J.E. (2017). A novel computational model predicts key regulators of chemokine gradient formation in lymph nodes and site-specific roles for CCL19 and ACKR4. J. Immunol. *199*, 2291–2304.

Johnson, L.A., Clasper, S., Holt, A.P., Lalor, P.F., Baban, D., and Jackson, D.G. (2006). An inflammation-induced mechanism for leukocyte transmigration across lymphatic vessel endothelium. J. Exp. Med. *203*, 2763–2777.

Karaman, S., Buschle, D., Luciani, P., Leroux, J.-C., Detmar, M., and Proulx, S.T. (2015). Decline of lymphatic vessel density and function in murine skin during aging. Angiogenesis *18*, 489–498.

Kissenpfennig, A., Henri, S., Dubois, B., Laplace-Builhe, C., Perrin, P., Romani, N., Tripp, C.H., Douillard, P., Leserman, L., Kaiserlian, D., et al. (2005). Dynamics and function of Langerhans cells in vivo: dermal dendritic cells colonize lymph node areas distinct from slower migrating Langerhans cells. Immunity *22*, 643–654.

Lämmermann, T., Bader, B.L., Monkley, S.J., Worbs, T., Wedlich-Söldner, R., Hirsch, K., Keller, M., Förster, R., Critchley, D.R., Fässler, R., and Sixt, M. (2008). Rapid leukocyte migration by integrin-independent flowing and squeezing. Nature *453*, 51–55.

Luther, S.A., Tang, H.L., Hyman, P.L., Farr, A.G., and Cyster, J.G. (2000). Coexpression of the chemokines ELC and SLC by T zone stromal cells and deletion of the ELC gene in the plt/plt mouse. Proc. Natl. Acad. Sci. U S A *97*, 12694–12699.

Martens, R., Permanyer, M., Werth, K., Yu, K., Braun, A., Halle, O., Halle, S., Patzer, G.E., Bosnjak, B., Kiefer, F., et al. (2020). Efficient homing of T cells via afferent lymphatics requires mechanical arrest and integrin-supported chemokine guidance. Nat. Commun. *11*, 1114.

Matti, C., D'Uonnolo, G., Artinger, M., Melgrati, S., Salnikov, A., Thelen, S., Purvanov, V., Strobel, T.D., Spannagel, L., Thelen, M., and Legler, D.F. (2020a). CCL20 is a novel ligand for the scavenging atypical chemokine receptor 4. J. Leukoc. Biol. *107*, 1137–1154.

Matti, C., Salnikov, A., Artinger, M., D'Agostino, G., Kindinger, I., Uguccioni, M., Thelen, M., and Legler, D.F. (2020b). ACKR4 recruits GRK3 prior to beta-arrestins but can scavenge chemokines in the absence of beta-arrestins. Front Immunol. *11*, 720.

Meyrath, M., Reynders, N., Uchanski, T., Chevigne, A., and Szpakowska, M. (2021). Systematic reassessment of chemokine-receptor pairings confirms CCL20 but not CXCL13 and extends the spectrum of ACKR4 agonists to CCL22. J. Leukoc. Biol. *109*, 373–376.

Ngo, V.N., Tang, H.L., and Cyster, J.G. (1998a). Epstein-Barr virus-induced molecule 1 ligand chemokine is expressed by dendritic cells in lymphoid tissues and strongly attracts naive T cells and activated B cells. J. Exp. Med. *188*, 181–191.

Ngo, V.N., Tang, H.L., and Cyster, J.G. (1998b). Epstein-Barr virus-induced molecule 1 ligand chemokine is expressed by dendritic cells in lymphoid tissues and strongly attracts naive T cells and activated B cells. J. Exp. Med. *188*, 181–191.

Nibbs, R.J.B., and Graham, G.J. (2013). Immune regulation by atypical chemokine receptors. Nat. Rev. Immunol. *13*, 815–829.

Norrmén, C., Ivanov, K.I., Cheng, J., Zangger, N., Delorenzi, M., Jaquet, M., Miura, N., Puolakkainen, P., Horsley, V., Hu, J., et al. (2009). FOXC2 controls formation and maturation of lymphatic collecting vessels through cooperation with NFATc1. J. Cell Biol. *185*, 439–457.

Nourshargh, S., and Alon, R. (2014). Leukocyte migration into inflamed tissues. Immunity *41*, 694–707.

Patel, D.D., Koopmann, W., Imai, T., Whichard, L.P., Yoshie, O., and Krangel, M.S. (2001). Chemokines have diverse abilities to form solid phase gradients. Clin. Immunol. *99*, 43–52.

Permanyer, M., Bosnjak, B., and Forster, R. (2018). Dendritic cells, T cells and lymphatics: dialogues in migration and beyond. Curr. Opin. Immunol. *53*, 173–179.

Petrova, T.V., Karpanen, T., Norrmén, C., Mellor, R., Tamakoshi, T., Finegold, D., Ferrell, R., Kerjaschki, D., Mortimer, P., Ylä-Herttuala, S., et al. (2004). Defective valves and abnormal mural cell recruitment underlie lymphatic vascular failure in lymphedema distichiasis. Nat. Med. *10*, 974–981.

Petrova, T.V., and Koh, G.Y. (2018). Organ-specific lymphatic vasculature: from development to pathophysiology. J. Exp. Med. *215*, 35–49.

Pham, T.H.M., Okada, T., Matloubian, M., Lo, C.G., and Cyster, J.G. (2008). S1P1 receptor signaling overrides retention mediated by Gαi-coupled receptors to promote T cell egress. Immunity *28*, 122–133.

Proulx, S.T., Luciani, P., Christiansen, A., Karaman, S., Blum, K.S., Rinderknecht, M., Leroux, J.-C., and Detmar, M. (2013). Use of a PEG-conjugated bright near-infrared dye for functional imaging of rerouting of tumor lymphatic drainage after sentinel lymph node metastasis. Biomaterials *34*, 5128–5137.

Russo, E., Teijeira, A., Vaahtomeri, K., Willrodt, A.-H., Bloch, J.S., Nitschké, M., Santambrogio, L., Kerjaschki, D., Sixt, M., and Halin, C. (2016). Intralymphatic CCL21 promotes tissue egress of dendritic cells through afferent lymphatic vessels. Cell Rep. *14*, 1723–1734.

Sabine, A., Agalarov, Y., Maby-El Hajjami, H., Jaquet, M., Hagerling, R., Pollmann, C., Bebber, D., Pfenniger, A., Miura, N., Dormond, O., et al. (2012). Mechanotransduction, PROX1, and FOXC2 cooperate to control connexin37 and calcineurin during lymphatic-valve formation. Dev. Cell *22*, 430–445.

Sabine, A., Bovay, E., Demir, C.S., Kimura, W., Jaquet, M., Agalarov, Y., Zangger, N., Scallan, J.P., Graber, W., Gulpinar, E., et al. (2015). FOXC2 and fluid

shear stress stabilize postnatal lymphatic vasculature. J. Clin. Invest. *125*, 3861–3877.

Salek, M.M., Sattari, P., and Martinuzzi, R.J. (2012). Analysis of fluid flow and wall shear stress patterns inside partially filled agitated culture well plates. Ann. Biomed. Eng. *40*, 707–728.

Sallusto, F., Palermo, B., Lenig, D., Miettinen, M., Matikainen, S., Julkunen, I., Forster, R., Burgstahler, R., Lipp, M., and Lanzavecchia, A. (1999a). Distinct patterns and kinetics of chemokine production regulate dendritic cell function. Eur. J. Immunol. *29*, 1617–1625.

Sallusto, F., Palermo, B., Lenig, D., Miettinen, M., Matikainen, S., Julkunen, I., Förster, R., Burgstahler, R., Lipp, M., and Lanzavecchia, A. (1999b). Distinct patterns and kinetics of chemokine production regulate dendritic cell function. Eur. J. Immunol. *29*, 1617–1625.

Schon, M.P., Zollner, T.M., and Boehncke, W.H. (2003). The molecular basis of lymphocyte recruitment to the skin: clues for pathogenesis and selective therapies of inflammatory disorders. J. Invest. Dermatol. *121*, 951–962.

Stein, J.V., Rot, A., Luo, Y., Narasimhaswamy, M., Nakano, H., Gunn, M.D., Matsuzawa, A., Quackenbush, E.J., Dorf, M.E., and von Andrian, U.H. (2000). The CC chemokine thymus-derived chemotactic agent 4 (TCA-4, secondary lymphoid tissue chemokine, 6Ckine, exodus-2) triggers lymphocyte function-associated antigen 1-mediated arrest of rolling T lymphocytes in peripheral lymph node high endothelial venules. J. Exp. Med. *191*, 61–76.

Tal, O., Lim, H.Y., Gurevich, I., Milo, I., Shipony, Z., Ng, L.G., Angeli, V., and Shakhar, G. (2011). DC mobilization from the skin requires docking to immobilized CCL21 on lymphatic endothelium and intralymphatic crawling. J. Exp. Med. *208*, 2141–2153.

Teijeira, A., Hunter, M.C., Russo, E., Proulx, S.T., Frei, T., Debes, G.F., Coles, M., Melero, I., Detmar, M., Rouzaut, A., and Halin, C. (2017). T cell migration from inflamed skin to draining lymph nodes requires intralymphatic crawling supported by ICAM-1/LFA-1 interactions. Cell Rep. *18*, 857–865.

Tomura, M., Hata, A., Matsuoka, S., Shand, F.H.W., Nakanishi, Y., Ikebuchi, R., Ueha, S., Tsutsui, H., Inaba, K., Matsushima, K., et al. (2014). Tracking and quantification of dendritic cell migration and antigen trafficking between the skin and lymph nodes. Sci. Rep. *4*, 6030.

Tomura, M., Honda, T., Tanizaki, H., Otsuka, A., Egawa, G., Tokura, Y., Waldmann, H., Hori, S., Cyster, J.G., Watanabe, T., et al. (2010). Activated regulatory T cells are the major T cell type emigrating from the skin during a cutaneous immune response in mice. J. Clin. Invest. *120*, 883–893.

Ulvmar, M.H., Hub, E., and Rot, A. (2011). Atypical chemokine receptors. Exp. Cell Res. *317*, 556–568.

Ulvmar, M.H., Werth, K., Braun, A., Kelay, P., Hub, E., Eller, K., Chan, L., Lucas, B., Novitzky-Basso, I., Nakamura, K., et al. (2014). The atypical chemokine receptor CCRL1 shapes functional CCL21 gradients in lymph nodes. Nat. Immunol. *15*, 623–630.

Veiga-Fernandes, H., Coles, M.C., Foster, K.E., Patel, A., Williams, A., Natarajan, D., Barlow, A., Pachnis, V., and Kioussis, D. (2007). Tyrosine kinase receptor RET is a key regulator of Peyer's patch organogenesis. Nature *446*, 547–51.

Vigl, B., Aebischer, D., Nitschké, M., Iolyeva, M., Röthlin, T., Antsiferova, O., and Halin, C. (2011). Tissue inflammation modulates gene expression of lymphatic endothelial cells and dendritic cell migration in a stimulus-dependent manner. Blood *118*, 205–215.

Vissers, J.L., Hartgers, F.C., Lindhout, E., Teunissen, M.B., Figdor, C.G., and Adema, G.J. (2001). Quantitative analysis of chemokine expression by dendritic cell subsets in vitro and in vivo. J. Leukoc. Biol. *69*, 785–793.

von Andrian, U.H., and Mackay, C.R. (2000). T-cell function and migration. Two sides of the same coin. N. Engl. J. Med. *343*, 1020–1034.

von der Weid, P.-Y., and Zawieja, D.C. (2004). Lymphatic smooth muscle: the motor unit of lymph drainage. Int. J. Biochem. Cell Biol. *36*, 1147–1153.

Vranova, M., Friess, M.C., Haghayegh Jahromi, N., Collado-Diaz, V., Vallone, A., Hagedorn, O., Jadhav, M., Willrodt, A.-H., Polomska, A., Leroux, J.-C., et al. (2019). Opposing roles of endothelial and leukocyte-expressed IL-7Rα in the regulation of psoriasis-like skin inflammation. Sci. Rep. *9*, 11714.

Weber, M., Hauschild, R., Schwarz, J., Moussion, C., de Vries, I., Legler, D.F., Luther, S.A., Bollenbach, T., and Sixt, M. (2013). Interstitial dendritic cell guidance by haptotactic chemokine gradients. Science *339*, 328–332.

Weber, M., and Sixt, M. (2013). Live Cell Imaging of Chemotactic Dendritic Cell Migration in Explanted Mouse Ear Preparations (Humana Press), pp. 215–226.

Werth, K., Hub, E., Gutjahr, J.C., Bosjnak, B., Zheng, X., Bubke, A., Russo, S., Rot, A., and Forster, R. (2021). Expression of ACKR4 demarcates the "perimarginal sinus," a specialized vascular compartment of the splenic red pulp. Cell Rep. *36*, 109346.

Woolf, E., Grigorova, I., Sagiv, A., Grabovsky, V., Feigelson, S.W., Shulman, Z., Hartmann, T., Sixt, M., Cyster, J.G., and Alon, R. (2007). Lymph node chemokines promote sustained T lymphocyte motility without triggering stable integrin adhesiveness in the absence of shear forces. Nat. Immunol. *8*, 1076–1085.

Yin, X., Truty, J., Lawrence, R., Johns, S.C., Srinivasan, R.S., Handel, T.M., and Fuster, M.M. (2010). A critical role for lymphatic endothelial heparan sulfate in lymph node metastasis. Mol. Cancer *9*, 316.

STAR★METHODS

KEY RESOURCES TABLE

REAGENT or RESOURCE	SOURCE	IDENTIFIER
Antibodies		
anti-mouse CD45-PE/Cy7	BioLegend	Cat# 103114; RRID: AB_312979
anti-mouse CD4-APC	BioLegend	Cat# 100412; RRID:AB_312697
anti-mouse CD8-FITC	BioLegend	Cat# 100706; RRID:AB_312745
anti-mouse/human B220-PerCP/Cy5.5	BioLegend	Cat# 103235; RRID:AB_893356
anti-mouse CD16/32	BioLegend	Cat# 101302; RRID:AB_312801
anti-mouse CD31 BV421	BD Bioscience	Cat# 562939; RRID:AB_2665476
anti-mouse LYVE-1 Alexa488	eBioscience	Cat# 53-0443-82; RRID:AB_1633415
anti-mouse CD31 PE	BioLegend	Cat# 102508; RRID:AB_312915
anti-mouse CD8 BV650	BioLegend	Cat# 100741; RRID:AB_11124344
anti-mouse CD11c APC	BioLegend	Cat# 117310; RRID:AB_313779
anti-mouse I-A/I-E-BV421	BioLegend	Cat# 107632; RRID:AB_2650896
anti-mouse Ep-CAM BV605	BioLegend	Cat# 118227; RRID:AB_2563984
Chemicals, peptides, and recombinant proteins		
PMA/12-O-tetradecanoylphorbol 13-acetate (TPA)	Sigma-Aldrich	Cat# P1585
Zombie Aqua	BioLegend	Cat# 423102
Cell Proliferation Dye eFluor670	eBioscience	Cat# 65-0840-85
CCL19-AF647	Almac	Cat# CAF-6
CCL21-Dy549	Dr. Daniel F. Legler (coauthor)	N/A
CCL21-Dy649	Dr. Daniel F. Legler (coauthor)	N/A
Critical commercial assays		
Trizol	Life Technologies	Cat# 15596026
EGM-2 BulletKit	Lonza	Cat# CC-3202
OptiMEM	Thermo Fisher Scientific	Cat# 31985070
Lipofectamine 2000	Thermo Fisher Scientific	Cat# 11668019
RNeasy Plus Micro Kit	Qiagen	Cat# 74034
Transcriptor First Strand cDNA Synthesis Kit	Roche	Cat# 04896866001
High-Capacity cDNA Reverse Transcription Kit	Fisher Scientific	Cat# 10400745
SensiFast Sybr Lo-Rox	Bioline	Cat# BIO-94020
PowerUp SYBR Green Master Mix	Thermo Fisher Scientific	Cat# A25776
Deposited data		
Analysed Data	Arasa et al. 2021	ArrayExpress: E-MTAB-9175
Analysed Data	Gonzalez-Loyola et al., 2021	GEO: GSE156320
Experimental models: Cell lines		
Human juvenile dermal LECs	PromoCell	Cat# 439Z007.2
Experimental models: Organisms/strains		
model organism: WT: C57BL/6	Janvier	N/A
model organism: ACKR4$^{GFP/GFP}$(KI) orACKR4$^{GFP/+}$(Het)	Heinzel et al., 2007	N/A
model organism: hCD2-dsRed	Veiga-Fernandes et al., 2007	N/A
model organism: Kikume Green-Red (KikGR)	Tomura et al., 2014	N/A
model organism: Foxc2$^{fl/fl}$xProx1-Cre^{ERT2}	Sabine et al., 2015	N/A
Oligonucleotides		
18s_Forward: AGGAATTCCCAGTAAGTGCG	Microsynth	N/A
18s_Reverse: GCCTCACTAAACCATCCAA	Microsynth	N/A

(*Continued on next page*)

Continued

REAGENT or RESOURCE	SOURCE	IDENTIFIER
Ackr4_Forward: TGCCATTCATTTCATTTTCCT	Microsynth	N/A
Ackr4_Reverse: CAAGACTGCTCCTCTCTGCC	Microsynth	N/A
Gja4_Forward: GGTGGGTAAGATCTGGCTGA	Microsynth	N/A
Gja4_Reverse: GGCCGTGTTACACTCGAAAT	Microsynth	N/A

RESOURCE AVAILABILITY

Lead contact

Further information and requests for recourses should be directed to and will be fulfilled by the lead contact, Dr. Cornelia Halin (cornelia.halin@pharma.ethz.ch).

Materials availability

Reagents are available upon request from the lead contact.

Data and code availability

This paper analyses existing, publicly available data. These accession numbers for the datasets are listed in the Key recourses table. This paper does not report original code. Any additional information required to reanalyse the data reported in this paper is available from the lead contact upon request.

EXPERIMENTAL MODEL AND SUBJECT DETAILS

Mice

C57BL/6 mice were purchased from Janvier (Le Genest-Saint-Isle, France) and bred in the animal facilities of ETH Zurich. ACKR4^{GFP} (Heinzel et al., 2007) and hCD2-dsRed (Veiga-Fernandes et al., 2007) mice were bred in the animal facilities of ETH Zurich. Kikume Green-Red (KikGR) mice were provided by Tomura et al. (Tomura et al., 2014). KikGRxACKR4^{GFP} mice were created by crossing ACKR4$^{GFP/GFP}$ mice with KikGR mice. Experiments were performed in age- and sex-matched male and female mice, as described in the corresponding STAR Methods sections. All mice were housed in the animal facilities of ETH Zurich. Animal experiments were approved and performed according to licenses of the Cantonal Veterinary Offices of the canton of Zurich canton (numbers 268/2014, 237/2016 and 239/2019) and the canton of Vaud (VD3334). To induce a lymphatic specific deletion of Foxc2 we used Foxc2$^{fl/fl}$xProx1-Cre^{ERT2} mice (Sabine et al., 2015). Each pup was injected 125 μg of tamoxifen (Sigma) in sunflower seed oil at postnatal day 4 and we sacrificed the mice at postnatal day 7.

Human lymphatic endothelial cell culture

Human LECs (PromoCell juvenile LECs, see Key resources table for details) were cultured in a humidified incubator (BINDER) at 37°C with 5% CO_2. For the culture of the cells the EGM-2 BulletKit medium was used (Lonza), with 5% FBS and all the supplements except VEGF-A. When 80-90% confluency was reached, cells were split or used in subsequent experiments, as described below.

METHOD DETAILS

TPA-induced inflammation

Mice were anesthetized by inhalation of 2.5% isoflurane. Ear thickness was measured using an ear caliper (Brütsch Rüegger, Urdorf, Switzerland) and 1μg of TPA (PMA/12-O-tetradecanoylphorbol 13-acetate, Sigma-Aldrich) in 10μL acetone (Sigma-Aldrich) was applied to each side of both ears. The next day lymphatic drainage was measured, KikGR lymphocytes were injected or mice were sacrificed for further analysis. In case of KikGRxACKR4^{GFP} mice, the ears were photoconverted 16 h after induction of TPA inflammation and mice sacrificed 6h after that.

Adoptive transfer of T cells in steady-state footpads

Experiments were performed in 7-10 week old age- and sex-matched male or female mice. To this end, LNs from 6-9 week old hCD2-dsRed mice were harvested and passed through a 40μm strainer to generate single cell suspensions. Up to 1*10^6 cells in 20μL PBS were injected into the footpads of recipient ACKR4$^{GFP/GFP}$ and WT mice. After 16h, recipient mice were sacrificed and popliteal LNs (both sides pooled per mouse) were harvested for FACS analysis. LNs were passed through a 70μm pre-separation filter (Miltenyi) directly into 5mL FACS tubes and centrifuged with filters still attached to ensure maximum cell yield. Cellularity was counted on a LUNA-FL Automated Fluorescence Cell Counter (Logos Biosystems, South Korea). Samples were stained in FACS buffer (PBS containing 2% FCS (Thermo Fisher) and 2 mM EDTA (Sigma-Aldrich)) for 20min on ice with the following antibodies

(all BioLegend): CD45-PE/Cy7 (clone 30-F11), CD4-APC (clone GK1.5), CD8-FITC (clone 53–6.7), B220-PerCP/Cy5.5 (clone RA3-6B2), CD16/32 (Fc-block) and zombie aqua (live/dead staining). Samples were centrifuged, resuspended in fresh FACS buffer and acquired on a CytoFLEX flow cytometer (Beckman Coulter) using CytExpert software and analysis was done using FlowJo software 10.4.1 (Tree star).

Adoptive transfer of T cells into TPA-inflamed ears

Experiments were performed in groups of 7-10 week old age- and sex-matched male or female mice. Lymphocytes from 6-9 week old KikGR mice were isolated for adoptive transfer into TPA-inflamed ears of ACKR4$^{GFP/GFP}$ and WT mice. Lymphocyte single cell suspension from KikGR mice were prepared by passing pooled LNs through 40μm cell strainers as described above, and up to 0.75*10^6 cells in 10μL PBS were injected at 3 different spots into the inflamed ears of recipient ACKR4$^{GFP/GFP}$ and WT mice. After 18h, recipient mice were sacrificed and auricular LNs (both sides pooled per mouse) were harvested for FACS analysis. LNs were passed through a 40μm cell strainer, the cellularity was counted on a LUNA-FL Automated Fluorescence Cell Counter (Logos Biosystems, South Korea) and the samples centrifuged. Single cell suspensions were stained in FACS buffer (PBS containing 2% FCS (Thermo Fisher) and 2 mM EDTA (Sigma-Aldrich)) for 20min on ice with the following antibodies (all BioLegend): CD45-APC/Cy7 (clone 30-F11), CD4-APC (clone GK1.5), CD8-BV-650 (clone 53–6.7), CD16/32 (Fc-block) and zombie aqua (live/dead staining). Samples were centrifuged, resuspended in fresh FACS buffer and acquired on a CytoFLEX flow cytometer (Beckman Coulter) using CytExpert software and analysis was done using FlowJo software 10.4.1 (Tree star).

CCL21 protein determination in mouse serum

Serum was collected from anesthetized groups of 8-12 week old, age-and sex-matched WT and ACKR4$^{GFP/GFP}$ KI mice and sent to Cytolab (Regensdorf, Switzerland) for analysis of CCL21 concentrations, using a multiplexed particle-based cytometric cytokine assay.

Lymphatic drainage assay

Experiments were either performed in 8-9 week old female mice (steady-state data) or in 11 – 13 week old male mice (TPA inflammation data). Lymphatic drainage in the ear was measured as described previously (Karaman et al., 2015; Proulx et al., 2013; Vranova et al., 2019). In brief, 3μL P20D800 (3μM synthesized as previously described (Vranova et al., 2019)) were injected intradermally into shaved ears of anesthetized mice (2.5% isoflurane inhalation anesthesia). Fluorescence was measured *in vivo* right after injection as well as 1, 2, 4, 6 and 24 h later with an IVIS imaging system (PerkinElmer). Image analysis was performed using Living Image 4.0 software (Perkin Elmer) and tracer clearance was determined as follows. For analysis, mouse ears were selected by drawing regions of interest (ROI) and subsequently fluorescence intensity was measured within each ROI. The background fluorescence intensity measured in un-injected ears was subtracted and the mean fluorescence intensity in each ROI was normalized to the mean fluorescence intensity right after injection (time point 0). These obtained normalized mean fluorescence intensities were plotted per mouse and fitted to a one-phase exponential decay model. This allowed half-life calculations, which represents tracer clearance from the mouse ear.

Whole mount immunofluorescence staining

Ear skin

Experiments on the general characterization of ACKR4-GFP expression in ear skin were performed in 10-15 week old female mice. Mice were euthanized, ears were shaved and small hair removed with Veet depilation cream. Ears were then split along the cartilage and excess cartilage removed with forceps. Fixation of ear skins for 2 h in 4% PFA in PBS was followed by washing for a total of 2 h (4 × 30min) with 0.3% triton-X in PBS. The tissue was then blocked for at least 1h with immunomix, containing 0.3% bovine serum albumin and 5% normal donkey serum in 0.3% triton-X/PBS. Ears were incubated overnight at 4°C with primary antibodies diluted in immunomix. The next day, ears were washed for a total of 2 h (4 × 30min) with 0.3% triton-X/PBS, incubated for 3h with appropriate secondary antibodies conjugated to Alexa-fluorophores (Invitrogen) and washed again (4 × 30 min) with 0.3% triton-X/PBS prior to mounting in Mowiol (Vector Laboratories).

Flank and leg collector

Experiments were performed in 6-12 week old male or female mice. For harvesting of leg collectors, the hind legs were shaved and hair was removed with Veet depilation cream. The skin was cut with a scalpel and carefully peeled away at the region of the collector. For harvesting of flank collectors, the skin and underlying tissue was separated from the intraperitoneal cavity with forceps to expose the flank collector. Collectors were then dissected using a stereomicroscope (Stemi 2000, Carl Zeiss Microscopy) with a blue light lamp (NIGHTSEA), to visualize endogenous GFP expressed in the collectors. Harvested collectors were pinned down into silica-coated wells for staining. Subsequent fluorescent staining was performed in analogy to the staining of ear skin.

Diaphragm and mesentery

Pups were sacrificed and diaphragm (analysis of p11) and intestine (analysis of p5) were collected and pinned down into silica-coated wells on cold PBS. Intestine was pinned in a circle, starting at the side that had been connected to the stomach, in order to span and expose mesentery for staining. Unpinned parts of the intestine and extra lung tissue were cut off. Tissues were fixed in 4% PFA/PBS at 4°C for 2 h followed by washing with PBS at room temperature (RT) and were then blocked for at least 2 h with immunomix at RT.

Staining with primary antibodies diluted in immunomix was carried out overnight at 4°C. Samples were then washed with PBS before staining with Alexa-conjugated secondary antibodies (Invitrogen) diluted in PBS for 3 h and washed again with PBS prior to mounting. Diaphragms were mounted with Mowiol while intestines were mounted with vectashield (Vector Laboratories) into chambered borosilicate coverglass system (Nunc).

The following primary antibodies were used for whole mount stainings: rat anti-mouse CD31 (clone MEC 13.3, BD Biosciences), polyclonal rabbit anti-mouse LYVE-1 (Angiobio), polyclonal goat anti-mouse CCL21 (R&D Systems), mouse anti-mouse α-smooth muscle actin e660 (clone 1A4, eBioscience), polyclonal goat anti-human PROX1 (R&D Systems), CD31 BV421, CD4 Alexa 647, CD45 PE. Images were acquired on Zeiss LSM 780 or 880 confocal microscopes (Carl Zeiss Microscopy) or a Leica TCS SP8 (Leica Microsystems) using the ZEN software (version 2.3; Carl Zeiss Microscopy) or Leica Application Suite LASX software (version 3.5.5.19976; Leica Microsystems), respectively.

For ACKR4 staining performed in WT or Foxc2$^{\Delta LEC}$ mice, p7 mesenteries were fixed with 4% PFA, washed with 10% sucrose and 20% sucrose and 10% glycerol, permeabilized with 0.5% Triton X-100 and blocked with 5% donkey serum. Samples were incubated overnight with ACKR4 antibody (Santa Cruz, sc-46835). Images were taken on a confocal Leica SP5 Tandem microscope (Leica Microsystems) and analyzed using Imaris and Adobe Photoshop software.

Adoptive transfer of e670 labelled T cells for section staining

Experiments were performed in 12 week old male mice. LNs and spleen were collected from WT mice and passed through a 40μm strainer. After centrifugation for 5 min at 340 g, cells were subjected to red blood cell lysis by incubation with ACK buffer for 5min on ice and washed with RPMI 1640 containing 10% FCS. CD4 (L3T4) microbeads (Miltenyi Biotec) were used for purification of CD4$^+$ cells. Cells were subsequently labeled with Cell Proliferation Dye eFluor670 (eBioscience) and 0.75*10^6 cells were injected into footpads of ACKR4$^{GFP/GFP}$ or WT mice together with 2 μg of anti-LYVE-1-Alexa488 antibody (eBioscience). Mice were sacrificed 24 h after injection and popliteal LNs collected and cryopreserved in OCT.

Chemokine production

Production of fluorescently labelled chemokine was previously described in (Artinger et al., 2021; Matti et al., 2020b). In brief, S6-tagged CCL19 or CCL21 was expressed in E.coli BL21 DE3, purified from inclusion bodies, refolded and affinity purified using a final C18 reverse phase HPLC step. Fluorophore linked to CoA was transferred to CCL19-S6 or CCL21-S6 using phosphopantetheinyl transferase Sfp (New England Biolabs) and labelled chemokine purified using C18 reverse phase HPLC.

Ex vivo chemokine uptake assay

Experiments were performed in 10-11 week old male mice. Mice were euthanized, ears were shaved and cleaned with ethanol. Ears were cut and split along the cartilage. The dorsal half of the ear was placed inside down into one well of a 24-well plate and incubated for 1 h with 500 ng/mL fluorescently labelled CCL19 in 250 μL RPMI containing 10% FCS and 1% penicillin/streptomycin at 37°C or 4°C or on ice. After 30 min 1 μL containing 0.2 μg anti-mouse CD31-PE (clone MEC13.3, BioLegend) antibody was directly added to the medium. Ear skin was washed with PBS, fixed with 2% PFA/PBS for 30min and washed again with PBS. Ears were mounted with Mowiol and imaged on a Zeiss LSM 780 or 880 confocal microscope (Carl Zeiss Microscopy) using ZEN software (version 2.3; Carl Zeiss Microscopy).

Analysis of SMA coverage

Experiments were performed in groups of 10 – 14 week old, age- and sex-matched male or female mice. For SMA quantification, the ROI in each image was selected based on CD31 staining and ACKR4^{GFP} reporter fluorescence resulting in CD31$^+$/ACKR4$^+$ regions and CD31$^+$/ACKR4$^-$ regions. After exclusion of areas containing blood vessels or other structures positive for SMA besides lymphatics, ROIs were applied to the SMA channel and the mean intensity was measured. In case of analysis of % area covered, a threshold for SMA staining was set before measurement and the same threshold was used for the entire dataset of one experiment. Analysis was performed in a blinded manner.

Analysis of T cell distribution within lymphatics by microscopy and FIJI (ImageJ)

Experiments were performed in groups of 6-10 week old (steady-state) or 8–10 week old (TPA-induced inflammation) age- and sex-matched male or female mice. Images were taken using a 20× objective on a Zeiss LSM 780 confocal microscope (Carl Zeiss Microscopy) using ZEN software (version 2.3; Carl Zeiss Microscopy), or on an Olympus upright confocal microscope using Olympus FV31S-SW software (version 2.3.1.163; Olympus Corporation). From the images, z-stacks were generated and regions of interest (ROIs) were defined in capillary and collector regions as follows: The ROI in each collector image was defined based on CD31 staining and ACKR4^{GFP} reporter fluorescence resulting in CD31$^+$/ACKR4$^+$ regions. The ROI in capillary regions was defined by the CD31 staining and characteristic lymphatic morphology. The ROI was subdivided in case of a larger blood vessels intersecting the capillary. The ROIs were then applied to the CD4 and CD45 channel and the number of double-positive cells within the vessel ROI was analysed, based on thresholding equally within each data set the fluorescence intensity and counting cells that had a diameter of at least 10μm. In addition, the length of the vessel segments was measured for the collector and capillary ROIs as well as the area for the capillary ROIs. The analysis was performed in a blinded manner, with always the same experimenter analyzing a particular dataset, allowing for relative comparison between the two genotypes.

Analysis of T cell migration in KikGRxACKR4^{GFP} mice by FACS

Experiments were performed in 7–14 week old, age-matched female mice. Acute TPA inflammation was induced in the ears and 16h later ears were photoconverted. To this end, mice were briefly anesthetized with isoflurane and ears were photoconverted at 100mW/cm^2 for 3min with a 405nm UV-LED (Opsytec Dr. Gröbel GmbH), allowing a full photoconversion through the whole depth of the ear. Mice were euthanized 6h after photoconversion and auricular LNs were taken and processed for FACS analysis. For steady-state experiments, mice were anesthetized with isoflurane and the lower area of the belly was shaved and photoconverted for 3 min as described above. Of note, the photoconversion depth did not reach the belly-dLNs. Other body-parts of the mouse remained light protected by covering it with aluminum foil. Belly-draining axillary and inguinal LNs were harvested 6h or 18h later and processed for FACS analysis. To this end, LNs were passed through 40μm cell strainers, washing the filter with FACS buffer (PBS containing 2% FCS (Thermo Fisher) and 2 mM EDTA (Sigma-Aldrich)). An aliquot of the single-cell suspension was taken to analyse the samples cellularity (LUNA-FL Automated Fluorescence Cell Counter, Logos Biosystems, South Korea) to enable normalization and absolute cell quantification. Samples were stained in FACS buffer for 20 min on ice with the following antibodies (all BioLegend): CD45-APC/Cy7 (clone 30-F11), CD4-AlexaFluor700 (clone GK1.5), CD8-BV650 (clone 53–6.7), CD11c-APC (clone N418), I-A/I-E-BV421 (clone M5/114.15.2), Ep-CAM-BV605 (clone G8.8), CD16/32 (Fc-block) and zombie aqua (live/dead staining). Samples were acquired on a CytoFLEX flow cytometer (Beckman Coulter) using CytExpert software and analysis was performed using FlowJo software 10.4.1 (Tree Star).

OCT sections and immunofluorescence of mouse ear skin sections

Experiments were performed in 8-12 week old female mice. Tissues were snap frozen in OCT and cut into 8 μm or 25 μm sections on a cryotome. In case of ear skin sections, ears from ACKR4$^{GFP/GFP}$ KI and ACKR4$^{GFP/+}$ Het mice were fixed in 2% PFA and subjected to a sucrose gradient prior to freezing in OCT. Sections were washed with TBS and blocked for 1h. In case of pankeratin staining, sections were blocked with immunomix containing 1% BSA and 5% normal donkey serum in 0.1% triton-X/PBS and stained overnight at 4°C with anti-Keratin pan antibody (Progen). Sections were washed and incubated with Alexa-conjugated secondary antibody (Invitrogen) for 30min at RT, washed and mounted with Mowiol (Vector Laboratories). In case of keratin 10 staining, sections were blocked with PBS containing 12% BSA and incubated with anti-keratin 10 antibody (BioLegend) for 1h at RT. Sections were then washed and incubated with Alexa-conjugated secondary antibody (Invitrogen) for 1h at RT, washed and mounted with Mowiol. In case of keratin 14 staining, sections were blocked with immunomix containing 1% BSA and 5% normal donkey serum in 0.1% triton-X/PBS and stained with polyclonal rabbit anti-keratin 14 antibody (Poly19053, BioLegend) for 1h at RT. Sections were then washed and incubated with Alexa-conjugated secondary antibody (Invitrogen) for 1h at RT, washed and mounted with Mowiol. Images were acquired with an Axioskop 2 mot plus microscope fitted with an AxioCam MRm camera and a Plan-NEOFLUAR 10×/0,30 44 03 30 objective (all Carl Zeiss Microscopy) using AxioVision Software (Carl Zeiss Microscopy).

In vivo chemokine uptake assay

Experiments with CCL19-AF647 (Almac) were performed in 10-12 week old female mice. Experiments with CCL21-Dy649 were performed in 6-8 week old male mice. Specifically, ACKR4$^{GFP/GFP}$ KI and ACKR4$^{GFP/+}$ Het mice were anesthetized by inhalation of anaesthesia (isoflurane, 2.5%) and 500ng CCL19-AF647 (Almac) or CCL21-Dy649 together with 1μg CD31-PE (clone MEC13.3, BioLegend) or CD31-AF594 (clone 390, BioLegend) were injected subcutaneously on the top of the paw in a total volume of 15 μL (control injections without fluorescently labeled chemokine were adjusted to 15 L with PBS). Mice were awake and motile for 30 min to allow drainage from the foot through the lymphatics. Mice were then euthanized and leg collectors were harvested, fixed with 2% PFA/PBS for 1 h at RT and washed with PBS prior to mounting with Mowiol. Images were taken on a Zeiss LSM 780 confocal microscope (Carl Zeiss Microscopy) using ZEN software (version 2.3; Carl Zeiss Microscopy), or on an Olympus upright confocal microscope using Olympus FV31S-SW software (version 2.3.1.163; Olympus Corporation), using a 20× objective.

FACS analysis of TPA-inflamed ears

Experiments were performed in 8–13 week old female mice. Ears of WT or ACKR4$^{GFP/GFP}$ KI mice were inflamed by topical application of TPA (described above) and mice euthanized after 16 h. Ears were ripped along the cartilage, cut into small pieces and digested in 4 mg/mL collagenase IV (Gibco) for 45 min at 37°C on a rotating wheel. Tissues were passed through a 40 μm cell strainer and washed with FACS buffer. Flow-Count Fluorospheres (Beckman Coulter) were added to the single-cell suspensions to allow for absolute cell quantification. Samples were stained on ice for 20 min with the following antibodies (all BioLegend unless otherwise stated): CD45-APC/Cy7 (clone 30-F11, Cat. 103116), CD4-PE (clone GK1.5, Cat. 100408), CD11c-PE/Cy7 (clone N418, Cat. 117318), I-A/I-E-BV421 (clone M5/114.15.2, Cat. 107632) and CD16/32 (Fc-block, Cat. 101302). Samples were acquired on a CytoFLEX flow cytometer (Beckman Coulter) using CytExpert software and analysis was performed using FlowJo software 10.4.1 (Tree Star).

In vitro flow experiments

Human LECs (PromoCell juvenile LECs) at passages 6-9 were seeded in 6-well plates, coated with 3 mg/mL collagen (PureCol, Advanced BioMatrix) 30min prior to seeding, at 250000 cells/well 24h before the start of the experiment and cultured in EBM2 medium (Lonza) containing kit components (EGM-2 BulletKit, without VEGFA, Lonza). Medium was exchanged and cells were subjected

to flow at 135 rpm for 48 h on an orbital shaker (WVR orbital shaker, advanced, Cat. 444-2908) (Salek et al., 2012). Half of the medium was replenished with fresh medium after 24h. For flow shear stress experiments with separate laminar, oscillatory (OSS) and static conditions, human intestinal lymphatic endothelial cells were seeded at confluence on fibronectin coated slides (μ-slide I 0.8 Luer, Ibidi) cultured for 24 h and subjected to flow (4 dynes/cm2) in a parallel plate flow chamber system (Ibidi Pump System, Ibidi) or kept under static conditions for 24 h, as previously described (Sabine et al., 2015).

In vitro chemokine uptake experiments in transfected LECs cell transfection experiments

Human LECs (PromoCell juvenile LECs) at passages 3-6 were seeded in 6-well plates (plastic from TPP for a readout by FACS, or glass from Cellvis for a readout by microscopy), coated with 3 mg/mL collagen (PureCol, Advanced BioMatrix) 30min prior to seeding, at 250,000 cells/well 24 h before the start of the experiment and cultured in EBM2 medium (Lonza) containing kit components (EGM-2 BulletKit, Lonza). At the transfection date medium was exchanged, and 1μg of plasmid (expressing ACKR4 or ACKR3 fused to EGFP under the CMV promotor; i.e. ACRK4-GFP and ACKR3-GFP) diluted in OptiMEM (Thermo Fisher Scientific) in 1:1 ratio with lipofectamine 2000 (Thermo Fisher Scientific) was added to the cells drop-wise. Cells were let to grow for 48h before subjecting them to the chemokine uptake assay. At the day of the chemokine uptake, cells were washed with PBS and starved for 30min with EBM2 medium (Lonza) containing 2% FBS and 1% antibiotic-antimycotic solution (Invitrogen). Cells were then incubated with 15nM of CCL21-Dy549 either at 37°C or on ice. After 1h, cells were washed with acidic wash buffer (100 mM NaCl and 50 mM glycin in dH2O, adjust to pH3) twice for 2 minutes. Finally, monolayers were washed with PBS. For a readout by FACS cells were detached using accutase (Sigma-Aldrich). Cells were collected and samples were acquired on a CytoFLEX flow cytometer (Beckman Coulter) using CytExpert software and analysis was done using FlowJo software (FlowJo, LLC). In the case of LECs transfected with either ACKR4-GFP or ACKR3-GFP, uptake of CCL21-Dy549 was evaluated on the GFP+ cells. For readout by microscopy, after the last wash cells were covered with mounting medium (vectashield with DAPI, Vector Laboratories) and imaged at an Olympus upright confocal microscope using Olympus FV31S-SW (version 2.3.1.163; Olympus Corporation), with a 20× objective and a 3× optical zoom.

In vitro chemokine uptake in flow-exposed LECs

Human LECs, which had been subjected to flow for 48 h or left at static condition, were washed with PBS and starved for 30min with EBM2 medium (Lonza) containing 2% FBS and 1% antibiotic-antimycotic solution (Invitrogen). Cells were then incubated with 10nM fluorescently labelled CCL19 (CCL19-AF647) (Matti et al., 2020b) or with or 15 nM of fluorescently labelled CCL21 (CCL21- Dy649), either at 37°C or on ice. After 1 h, cells were washed with acidic wash buffer (100 mM NaCl and 50 mM glycin in dH2O, adjust to pH3) for no more than 1 minute. In the case of LECs incubated with CCL21-Dy649, two acidic washes of 2 min each were performed. Next monolayers were washed with PBS and detached using accutase (Sigma-Aldrich). Cells were collected and samples were acquired on a CytoFLEX flow cytometer (Beckman Coulter) using CytExpert software and analysis was done using FlowJo software (FlowJo, LLC).

Gene expression analysis of in vitro-cultured human LECs

Cells were grown as described for *in vitro* flow experiments. For the detection of flow induced genes, RNA was isolated using Trizol (Life Technologies Cat. 15596026) or using the RNeasy Plus Micro Kit (Qiagen Cat. 74034). cDNA was generated using the Transcriptor First Strand cDNA Synthesis Kit (Roche, Cat. 04896866001) or the High-Capacity cDNA Reverse Transcription Kit (Fisher Scientific Cat. 10400745). Quantitative PCR was performed on reversely transcribed RNA using SYBR green reagents (Bioline SensiFast Sybr Lo-Rox Cat. BIO-94020) or PowerUp SYBR Green Master Mix (Thermo Fisher Scientific Cat. A25776). Gene expression analysis was conducted using the following primers (Microsynth AG): *18s* (forward AGGAATTCCCAGTAAGTGCG, reverse GCCTCAC TAAACCATCCAA); human *ackr4* (forward TGCCATTCATTTCATTTTCCT, reverse CAAGACTGCTCCTCTCTGCC); human *gja4* (forward GGTGGGTAAGATCTGGCTGA, reverse GGCCGTGTTACACTCGAAAT) and performed on a QuantStudio 3 or 7 Flex system (Applied Biosciences).

Stereomicroscopic analysis of GFP expression

Experiments were performed in 5 – 6 week old male or female ACKR4$^{GFP/GFP}$ or ACKR4$^{GFP/+}$ Het mice. Animals were euthanized and carefully dissected under a Zeiss AxioZoom V16 stereomicroscope fitted with a QImaging OptiMOS sCMOS camera (QImaging) combined with a light-emitting diode illumination system pE-4000 (CoolLED Ltd.). Images were acquired using Zen2 Blue Edition software (Carl Zeiss Microscopy).

QUANTIFICATION AND STATISTICAL ANALYSIS

Data sets were analysed using Student's t-test when comparing 2 groups or 1-way ANOVA followed by Bonferroni corrections when analyzing more than 2 groups. These results are presented as mean ± SEM. Chi square analysis was performed on data for T cell distribution within vessel segments. Mann-Whitney test was used for analysis of T cell numbers within vessel segments. These results are presented as median ± SEM. Statistical significance was assumed when $p < 0.05$. Statistical analysis was performed with Prism 7 and 9 (GraphPad Software Inc.) and graphs were generated with the same software.